JOURNAL OF GUIDANCE, CONTROL, AND DYNAMICS
Vol. 47, No. 10, October 2024

Design of Robust Ballistic Landings on the Secondary of a Binary Asteroid

Iosto Fodde,* Jinglang Feng,† and Massimiliano Vasile‡
University of Strathclyde, Glasgow, Scotland G1 1XJ, United Kingdom
and
Jesús Gil-Fernández§
European Space Agency, 2200 AG Noordwijk, The Netherlands

https://doi.org/10.2514/1.G007786

ESA's Hera mission aims to visit binary asteroid Didymos in late 2026, investigating its physical characteristics and the result of NASA's impact by the DART spacecraft in more detail. Two CubeSats onboard Hera plan to perform a ballistic landing on the secondary of the system, called Dimorphos. For these types of landings the translational state during descent is not controlled, reducing the spacecraft's complexity but also increasing its sensitivity to deployment maneuver errors and dynamic uncertainties. This paper introduces a novel methodology to analyze the effect of these uncertainties on the dynamics of the lander and design a trajectory that is robust against them. This methodology consists of propagating the uncertain state of the lander using the nonintrusive Chebyshev interpolation (NCI) technique, which approximates the uncertain dynamics using a polynomial expansion. The results are then analyzed using the pseudo-diffusion indicator. This indicator is derived from the coefficients of the polynomial expansion, which quantifies the rate of growth of the set of possible states of the spacecraft over time. The indicator is used here to constrain the impact velocity and angle to values that allow for successful settling on the surface. This information is then used to optimize the landing trajectory by applying the NCI technique inside the transcription of the problem. The resulting trajectory increases the robustness of the trajectory compared to a conventional method, improving landing success by 20% and significantly reducing the landing footprint.

Nomenclature

a, b, c	=	ellipsoidal shape parameters, m
C_{lm}, S_{lm}	=	spherical harmonics Stokes coefficients
$P_{n,d}$	=	polynomial of order n with d variables
R	=	spherical harmonics reference radius, m
T_i	=	Chebyshev polynomial of the first kind of order i
$\boldsymbol{u}$	=	decision vector
$\boldsymbol{v}^{-/+}$	=	incoming/outgoing landing velocity vector, m/s
$\boldsymbol{x}$	=	spacecraft translational state, m, m/s
$\boldsymbol{\beta}$	=	model parameter vector
$\tilde{\gamma}$	=	pseudo-diffusion indicator
δ, λ	=	geographical latitude and longitude, deg
ϵ	=	coefficient of restitution
θ_{land}	=	impact angle, deg
μ	=	gravitational parameter, m^3/s^2
μ_m	=	mass ratio, $m_2/(m_1 + m_2)$
Σ	=	covariance matrix
σ	=	standard deviation
Ω	=	uncertainty set

Received 13 June 2023; accepted for publication 14 June 2024; published online 20 August 2024.

*Ph.D. Student, Mechanical and Aerospace Engineering, 75 Montrose Street; iosto.fodde@strath.ac.uk; currently Postdoctoral Researcher, Department of Aerospace Science and Technology, Politecnico di Milano, Via La Masa, 34, 20156, Milan; iosto.fodde@polimi.it.

†Chancellor's Fellow, Mechanical and Aerospace Engineering, 75 Montrose Street; jinglang.feng@strath.ac.uk.

‡Professor, Mechanical and Aerospace Engineering, 75 Montrose Street; massimiliano.vasile@strath.ac.uk.

§GNC Engineer, Systems Department: Guidance, Navigation and Control Section (TEC-SAG), Keplerlaan 1, P.O. Box 299; jesus.gil.fernandez@esa.int.

I. Introduction

MISSIONS to minor solar system bodies like asteroids, comets, and planetary moons provide several benefits: increasing our knowledge on the origins of the solar system, improving our capability to defend ourselves against potentially hazardous objects, and leading to future use of the resources located within these bodies [1]. One of these missions, NASA's Double Asteroid Redirection Test (DART), part of the Asteroid Impact and Deflection Assessment (AIDA) collaboration between NASA and ESA, successfully impacted the secondary asteroid of binary system Didymos (68503), called Dimorphos. This mission showed the potential of a kinetic impactor for deflecting an asteroid heading toward Earth as it was able to change Dimorphos's orbital state around the primary asteroid [2]. ESA's Hera spacecraft will arrive in late 2026 to do a more in-depth investigation of the result of the impact and perform additional scientific measurements of the asteroids. Two CubeSats are located onboard of Hera, called Milani and Juventas, which act as additional scientific payloads, ending their missions with a landing on Dimorphos [3].

Landings on the surface of asteroids are incredibly valuable in terms of scientific return, as the spacecraft–surface interaction provides direct information on the internal structure and material properties of the asteroid while their instruments can do some in situ measurements to characterize the asteroid in more depth. Various previous missions performed landings or surface touchdowns, among them the Hayabusa mission [4], Rosetta [5], Hayabusa 2 [6], and OSIRIS-REx [7]. Precise landings require a complex and precise guidance, navigation, and control (GNC) system, increasing the complexity of the spacecraft. As the Hera CubeSats have a limited size and mass budget, a dedicated landing GNC system might not be feasible. Therefore, ballistic landings, i.e., with no closed-loop control of the translational state during descent, are good options for the landing maneuver. The main drawbacks of ballistic landings are their sensitivity to errors in the deployment maneuver and uncertainties in the dynamic parameters [8]. Therefore, when designing ballistic landing trajectories, the impact of uncertainties needs to be taken into account.

The complex dynamics due to the large influence of the primary, nonspherical shape of both bodies and the low gravitational forces make the landing trajectory design difficult. Initial studies on ballistic landing trajectories investigated deploying the spacecraft on natural manifold trajectories from the L_2 point of binary asteroid systems

[9–12]. Specifically, the authors of Ref. [13] looked into landing on Dimorphos using this methodology, but deploying at further, i.e., safer, distances away from the L_2 point. This technique involves deploying the spacecraft with a higher velocity onto a stable manifold toward L_2 and onto the unstable manifold (ensuring transfer to the inward branch of the manifold by increasing the initial velocity), which intersects with the surface of Dimorphos. These trajectories were shown to have low touchdown velocities and a high likelihood for settling on the surface, but were also found to be sensitive to uncertainties in the deployment maneuver and surface characteristics. To generalize these low-energy landing trajectories to be able to land all across the surface of the secondary, approaches involving propagating vertical landing trajectories backward in combination with a bisection-based method to find the minimum energy trajectory for a certain location were proposed in [8,14] The bouncing and surface motion of landers has also been investigated in detail in [15–19]. These studies highlight the importance of implementing accurate and efficient models for the dynamics of this phase of the landing trajectory design, and it can have a large influence on to the lander settling location and success of the landing itself.

Besides the complex dynamics, another problem in the trajectory design process is the highly uncertain environment in which the spacecraft needs to operate, as ground-based observations are not able to determine the asteroid's property with a high degree of accuracy [20]. Most previous missions dedicated several months of mission time at arrival, reducing the uncertainties by observing the system from large distances; see, e.g., the NEAR mission [21]. This increases the mission costs as intensive ground segment efforts are required, which does not necessarily scale down for smaller CubeSat missions. Thus, other techniques to deal with the inherent uncertainties should be explored. Often, these uncertainties are included after a nominal trajectory has already been designed to check the sensitivity of the trajectory to them. This decoupling is inefficient and can lead to worse performances as conservative safety margins are added [22]. Furthermore, conventional methods for this process, like linear covariance analysis, require the dynamics to be close to linear and/or the uncertainties to be small. More accurate techniques like the Monte Carlo method, on the other hand, require a large amount of samples to be propagated through the dynamics (error is roughly proportional to $1/\sqrt{N}$, where N is the amount of samples) [23]. Hence, this technique is not numerically efficient enough to be used in applications like determining phase space structures or trajectory optimization algorithms, which require large amount of initial conditions to be investigated and thus need more efficient uncertainty propagation and quantification techniques.

This study introduces a novel methodology for the analysis and design of ballistic landing trajectories, which takes into account the uncertainties present in the system throughout the full process. The proposed method first uses nonintrusive Chebyshev interpolation (NCI) to propagate the uncertain state of the lander for a large amount of landing conditions (velocity magnitude and direction). For each landing condition, the rate of growth of the uncertain state is then determined using the pseudo-diffusion indicator [24]. This information allows for the discovery of conditions that lead to a high probability of a successful landing, which is then used to design the final ballistic landing trajectory. This trajectory is again designed with the uncertainties taken into account by applying NCI inside the trajectory optimization transcription and minimizing the final variance of the state.

The paper is structured as follows: First, Sec. II discusses the specific dynamic models used here. Then, Sec. III explains the uncertainty propagation technique used as well as introduces the pseudo-diffusion indicator, which is used to map the different dynamic regimes and quantify the influence of uncertainties on the landers motion. Afterward, these methods are applied to the surface motion in Sec. IV, investigating the optimal conditions for settling on the asteroid surface and how the uncertain surface conditions influence this. Then, Sec. V investigates what the minimal touchdown velocity is for different landing locations. Finally, Sec. VI applies the uncertainty propagation method inside a trajectory optimization scheme, using all the information from the previous analyses to design a robust landing trajectory. The work is then concluded in Sec. VII.

II. Binary Asteroid Dynamics

The two bodies part of the Didymos (68503) binary asteroid system are the main asteroid Didymos with a diameter of around 780 m and the secondary asteroid Dimorphos of around 164 m, which is the target body for the landing discussed in this work. The physical parameters determined from the pre- and postimpact observations of the system can be found in Table 1. The effect of the DART impact on Dimorphos is mainly seen in the change of orbital period of 32 minutes and thus a change in the semimajor axis of 48 m [2]. The eccentricity is also slightly increased, to a value of around 0.03. As this value is low enough to not alter the dynamics of the system significantly for the problem considered in this work, a circular orbit will be assumed for Dimorphos. Changes to the shape and mass of Dimorphos are also expected due to the impact [25]. However, these changes can only be measured once the Hera spacecraft arrives at the system, and thus the shape and mass of Dimorphos used here are based on the pre-impact measurements.

As the asteroids are assumed to be in a (close to) circular orbit around the center of mass of the system and the mass of the CubeSat is negligible compared to the masses of both asteroids, the circular restricted three-body problem (CR3BP) is used to model the dynamics. The equations of motion for this model are stated in a synodic reference frame, which rotates together with the orbital period of the system. This results in both bodies being stationary in this reference frame, where the x axis is defined to be pointing in the direction of Dimorphos, the z axis in the direction of the orbit normal, and the y axis completing the right-handed frame. All variables are then made dimensionless using the mass parameter $\mu_m = m_2/(m_1 + m_2)$, the body separation distance R, and the time constant $1/n$ (where n is the mean motion of Dimorphos). This results in the following set of equations describing the motion of the third body [28]:

$$\begin{cases} \ddot{x} - 2\dot{y} &= \dfrac{\partial U}{\partial x}, \\ \ddot{y} + 2\dot{x} &= \dfrac{\partial U}{\partial y}, \\ \ddot{z} &= \dfrac{\partial U}{\partial z} \end{cases} \tag{1}$$

Table 1 Relevant physical parameters of the Didymos system, taken from [26,27]

Parameter	Value and uncertainty
System mass	$5.28(\pm 0.54) \cdot 10^{11}$ kg
Mass ratio	0.0093 ± 0.0013
Didymos ellipsoidal axes	$a = 399 \pm 7.5$ m, $b = 392 \pm 7.5$ m, $c = 380 \pm 7.5$ m
Didymos rotational period	2.26 h ± 0.0001 h
Dimorphos ellipsoidal axes	$a = 107 \pm 2$ m, $b = 79 \pm 4$ m, $c = 66 \pm 2$ m
Dimorphos orbital period (pre-impact)	11.92148 ± 0.000044 h
Dimorphos orbital period (postimpact)	11.372 ± 0.0055 h
Body separation distance (pre-impact)	1.206 ± 0.035 km
Body separation distance (post-impact)	1.144 ± 0.07 km

Table 2 Gravitational harmonics coefficients calculated from Eqs. (3–7)

Coefficient	Didymos	Dimorphos
C_{20}	−0.016	−0.13
C_{22}	0.0018	0.035
C_{40}	5.5e−4	0.042
C_{42}	−2.06e−5	−3.30e−3
C_{44}	5.91e−7	2.22e−4

The potential U includes both the rotational terms stemming from the noninertial reference frame used and the gravitational forces acting on the third body. For the close proximity motion that is mostly relevant during the landing operations, the gravitational forces from both asteroids dominate the dynamics compared to other forces like the solar radiation pressure or the solar gravity [29]. Thus, only these forces are considered. To model the nonspherical gravitational effects of the body, the spherical harmonics model is used, where the potential is given as follows [30]:

$$U_g(r,\delta,\lambda) = \frac{\mu}{r}\sum_{l=0}^{\infty}\sum_{m=0}^{l}\left(\frac{R}{r}\right)^{l} P_{lm}(\sin\delta)[C_{lm}\cos m\lambda + S_{lm}\sin m\lambda] \tag{2}$$

where r is the radial distance from the center of the body, δ is the latitude, λ is the longitude, μ is the gravitational coefficient of the body, R is a normalized radius [which is taken as $\sqrt{3/(1/a^2+1/b^2+1/c^2)}$], P_{lm} are the associated Legendre functions (their expressions can be found in [31]), and C_{lm} and S_{lm} are the Stokes coefficients, which represent the mass distribution of the body. As both Didymos and Dimorphos are roughly shaped as an ellipsoid, the Stokes coefficients can be determined analytically as follows [32]:

$$C_{20} = \frac{1}{5R^2}\left(c^2 - \frac{1}{2}(a^2+b^2)\right) \tag{3}$$

$$C_{22} = \frac{1}{20R^2}(a^2-b^2) \tag{4}$$

$$C_{40} = \frac{15}{7}(C_{20}^2 + 2C_{22}^2) \tag{5}$$

$$C_{42} = \frac{5}{7}C_{20}C_{22} \tag{6}$$

$$C_{44} = \frac{5}{28}C_{22}^2 \tag{7}$$

where a, b, and c are the three different axes describing the ellipsoidal shape of the body (see Table 1). The specific values of the coefficients for both bodies can be found in Table 2. One significant disadvantage of the spherical harmonics model is that there is a possibility of the model diverging for $r < R$ [31]. However, in the case of a triaxial ellipsoid, there is a certain condition that guarantees global convergence, namely, that $a < c\sqrt{2}$ [32]. As this condition holds for the shape of both Didymos and Dimorphos, the spherical harmonics model can be used globally.

III. Uncertain Dynamics Analysis

The motion of the spacecraft during all phases of the landing is severely affected by uncertainties. The maneuver from the operational orbit to the landing trajectory is affected by the uncertainty in the state of the spacecraft stemming from the navigation system and the error in the direction and magnitude of the ΔV maneuver. During the following ballistic flight, the imperfect dynamic modeling of the system will cause the spacecraft to move away from the nominal trajectory and behave differently than expected. Finally, at touchdown the uncertainties in the surface properties and the presence of rocks and boulders will cause the spacecraft to move across the surface of the body in an unpredictable manner. It is therefore necessary to consider all these uncertainty sources during the design and execution of the landing maneuver.

This section discusses first a method to propagate the uncertainties through the system and obtain a polynomial expansion of the uncertain and dynamics. Afterward, a novel indicator based on this polynomial expansion is discussed, which allows for the characterization of the effect of uncertainties on the motion of the spacecraft.

A. Nonintrusive Chebyshev Interpolation

Consider an initial value problem defined as follows:

$$\begin{cases} \dot{\boldsymbol{x}} = \boldsymbol{f}(\boldsymbol{x}(t),\boldsymbol{\beta},t) \\ \boldsymbol{x}(t_0) = \boldsymbol{x}_0 \end{cases} \tag{8}$$

where t is the time, $\boldsymbol{x}$ is the state vector, and $\boldsymbol{\beta}$ is a vector containing the dynamic model parameters. In this work, both the initial state $\boldsymbol{x}_0$ and model parameters $\boldsymbol{\beta}$ are uncertain. Consider a set of N realizations or samples from the uncertainties: $[\boldsymbol{x}_{0,1},\boldsymbol{\beta}_1,\ldots,\boldsymbol{x}_{0,N},\boldsymbol{\beta}_N]$. Each sample can be propagated through Eq. (8) until time t_f, which results in a set of trajectories $\boldsymbol{x}_i(t_f) = \phi_i(\boldsymbol{x}_{0,i},\boldsymbol{\beta}_i,t_f)$.

The set of all possible initial states, considering all the uncertainties in the system, is given as follows:

$$\Omega_{\boldsymbol{x}_0} = \{\boldsymbol{x}(t_0,\boldsymbol{\xi}) | \boldsymbol{\xi} \in \Omega_{\boldsymbol{\xi}}\} \tag{9}$$

where the uncertainties are given by $\boldsymbol{\xi} = [\boldsymbol{x}_0,\boldsymbol{\beta}]$. The propagated set representing all possible trajectories at time t from the realizations of the uncertainty vector $\boldsymbol{\xi}$ within the uncertainty set $\Omega_{\boldsymbol{\xi}}$ is given by

$$\Omega_t(\boldsymbol{\xi}) = \{\boldsymbol{x}(t) = \phi(\boldsymbol{\xi},t) \mid \boldsymbol{\xi} \in \Omega_{\boldsymbol{\xi}}\} \tag{10}$$

To understand the effect of the uncertainties on this system, an analytical expression of this set needs to be obtained.

Recently, both intrusive and nonintrusive methods based on the polynomial expansion of the uncertain variables have become more popular for uncertainty propagation (see, e.g., [33,34]). These methods can have their accuracy and numerical efficiency tuned using the amount of propagated samples and/or the polynomial order of the fitted model. The nonintrusive methods are especially interesting as they can treat the dynamics as a black box and can create an analytical representation of the dynamics using significantly fewer samples than is needed for traditional Monte Carlo (MC) methods. This makes them attractive for dynamics that have complex, nonlinear equations of motion with uncertain and/or stochastic elements.

If $\boldsymbol{x}_t$ is continuous in $\boldsymbol{\xi}$ and the set is compact, $\Omega_t(\boldsymbol{\xi})$ can be approximated using a polynomial function:

$$\tilde{\Omega}_t(\boldsymbol{\xi}) = P_{n,d}(\boldsymbol{\xi}) = \sum_{i=0}^{\mathcal{N}} c_i(t)\alpha_i(\boldsymbol{\xi}) \tag{11}$$

where $\alpha_i(\boldsymbol{\xi})$ are a set of multivariate polynomial basis functions, $c_i(t)$ are the corresponding coefficients, and $\mathcal{N} = \binom{n+d}{d}$ is the number of terms of the polynomial, where n is the degree of the polynomial and d is the number of variables. Chebyshev polynomials are often used for approximation purposes as they have several attractive numerical properties [35]. These polynomials have been previously used in an astrodynamics setting as well in [36,37]. This work follows a similar approach as [34,36] and uses a Chebyshev polynomial basis together with a Smolyak sparse grid sampling approach to obtain the polynomial from Eq. (11), which is hereafter called the NCI method.

The Smolyak sparse grid was developed in [38] and selects a set of points based on the extrema of Chebyshev polynomials. An important aspect is that they do not suffer the curse of dimensionality, as the number of points grow polynomially with the dimension of the problem instead of exponentially. A more in-depth explanation of this method for uncertainty propagation is given in [36].

Given the propagated samples, the coefficients of the polynomial can be obtained by inverting the following system:

$$HC = Y \tag{12}$$

where

$$H = \begin{bmatrix} T_{i_1}(\boldsymbol{\xi}_1) & \dots & T_{i_s}(\boldsymbol{\xi}_1) \\ \vdots & \ddots & \vdots \\ T_{i_1}(\boldsymbol{\xi}_s) & \dots & T_{i_s}(\boldsymbol{\xi}_s) \end{bmatrix}, C = \begin{bmatrix} c_{i_1} \\ \vdots \\ c_{i_s} \end{bmatrix}, Y = \begin{bmatrix} y_1 \\ \vdots \\ y_s \end{bmatrix} \tag{13}$$

where $s = \mathcal{N} = \binom{n+d}{d}$; $\boldsymbol{\xi}_1, \dots, \boldsymbol{\xi}_s$ are the Smolyak sparse grid points; and Y is the vector containing all the corresponding propagated samples $y_i = \phi_i(\boldsymbol{\xi}_i, t)$.

To show the effect of different sampling approaches on the accuracy of the coefficients obtained from inverting Eq. (12), an analysis is done on a typical landing trajectory where there is a ballistic flight phase and a landing and surface motion phase. The complexity in the dynamics stemming from the moment of landing can be particularly difficult on the approximation. The accuracy is measured by taking a set of uniformly sampled points and comparing the samples at different times along the trajectory between an MC approach and the polynomial expansion of Eq. (11). Both the root-mean-squared error (RMSE) and maximum error over all samples are calculated. The RMSE is calculated as follows:

$$\mathrm{RMSE} = \sqrt{\frac{1}{N_s}\sum_{i=1}^{N_s}(\hat{x}_i - x_i)^2} \tag{14}$$

where $\hat{x}_i$ is the NCI-calculated state and x_i is the MC state at the same point in time. As a comparison against the Smolyak sparse grid, the Latin hypercube sampling (LHS) method is used. The LHS method divides the sampling space into several uniformly spaced subspaces in which a random sample is taken for each individual subspace. The resulting RMSE and maximum error along the trajectory are given in Fig. 1. Both methods show relatively equal accuracy during the ballistic phase. However, the sparse grid method handles the landing much better compared to the LHS method, for which a large jump in RMSE and max error happens.

Once a polynomial model of the states of the system, at a given time, is available, one can use the polynomial expansion to extract useful information on the evolution of the dynamics without the need of expensive MC simulations. In the following, we will show how one can derive a quantification of the rate of divergence of an ensemble of trajectories, induced by multiple realizations of the uncertain quantities, directly from the coefficients of the NCI model.

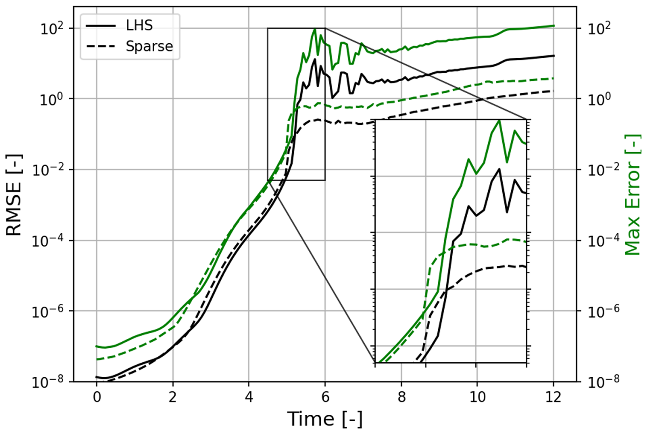

Fig. 1 LHS sampling accuracy compared against the Smolyak sparse grid accuracy.

B. Pseudo-Diffusion Indicator

In the analysis of dynamic systems, dynamic indicators are often used to identify different dynamic structures and other dynamic phenomena like chaos, coherent structures, and/or diffusive behavior. These indicators are often based on the sensitivity of initial conditions to small perturbations, examining how these perturbations grow over time. Examples of these indicators are the finite time Lyapunov exponent [39] and the fast Lyapunov indicator [40]. In the case that the dynamics contains uncertain parameters, the indicators would need to be recalculated for each realization of the uncertainties, and a statistical analysis would need to be performed over all the different values of the indicator. This can be numerically inefficient as the amount of initial conditions to be analyzed grows and the uncertainties become larger. Therefore, recently there have been several developments of indicators that can be easily derived from polynomial models like the NCI and capture the effect of uncertainty and stochastic processes (see, e.g., [41–43]).

In this work, we want to identify target landing conditions that lead to a small divergence of the post-touchdown trajectories under the effect of uncertainty on the contact dynamics. Therefore, the pseudo-diffusion indicator developed in [24] is used to characterize the landing conditions as it measures the rate of divergence of an ensemble of trajectories induced by multiple realizations of the uncertainty set. In the case of a (partial) landing, the touchdown conditions are uncertain, but it is desirable that the post-touchdown trajectories are poorly affected by such an uncertainty and thus have a low degree of divergence.

The pseudo-diffusion indicator is based on the fact that, for a generic random-walk-like process in the univariate case, the mean-squared displacement of an ensemble of trajectories grows according to the following equation [44]:

$$\sigma^2 = \mathbb{E}\left[(x(t) - \bar{x}(t))^2\right] \approx K_\gamma t^\gamma \tag{15}$$

where K_γ is the diffusion coefficient, γ is the diffusion exponent, and $\bar{x}$ is a reference position. Then, using the fact that the state is expanded using the polynomial of Eq. (11) and using the orthogonality of the Chebyshev polynomials used as the basis for the polynomial expansion, it can be shown that the variance of the state can be calculated as follows:

$$\begin{aligned}\sigma^2(t) &\asymp \mathbb{E}\left[(\tilde{x}(t) - \bar{\tilde{x}}(t))^2\right] \\ &= \int_{\Omega_\xi}\left(\sum_{i,|i|\neq 0} c_i(t)T_i(\boldsymbol{\xi})\right)\cdot\left(\sum_{i,|i|\neq 0} c_i(t)T_i(\boldsymbol{\xi})\right)\rho(\boldsymbol{\xi})d\xi \\ &= \sum_{i,|i|\neq 0}\kappa_i\, c_i^2(t)\end{aligned} \tag{16}$$

where $\kappa = |\, \boldsymbol{i} \,|\, !\sqrt{2\pi}$. Therefore,

$$\sum_{i,|i|\neq 0}\kappa_i\, c_i^2(t) = K_\gamma t^\gamma \tag{17}$$

Assuming large t, γ can be approximately found using the following expression:

$$\gamma \approx \tilde{\gamma}_o = \frac{\log\left(\sum_{i,|i|\neq 0}\kappa_i\, c_i^2(t) + 1\right)}{\log t} \tag{18}$$

where $\tilde{\gamma}_o$ is called the pseudo-diffusion exponent.

In this work, a slightly altered version of the pseudo-diffusion indicator is used with respect to the definition given in Eq. (18). The expression for the mean-squared displacement is altered to measure the displacement with respect to the desired touchdown location x_{td} as follows:

$$\mathbb{E}[(x(t)-x_{td})^2] = \mathbb{E}[x(t)^2] - 2x_{td}\mathbb{E}[x(t)] + x_{td}^2 \tag{19}$$

$$\approx \sum_{i,|i|\neq 0} \kappa_i \, c_i^2(t) + (c_0 - x_{td})^2 \tag{20}$$

In the multivariate case, this can be shown to be equal to

$$\mathbb{E}[|\boldsymbol{x}(t) - \boldsymbol{x}_{td}|^2] \approx \sum_{\boldsymbol{i},|\boldsymbol{i}|\neq 0} \kappa_{\boldsymbol{i}} \, |\boldsymbol{c}_{\boldsymbol{i}}(t)|^2 + (\boldsymbol{c}_0 - \boldsymbol{x}_{td})^2 \tag{21}$$

This results in the following definition for the pseudo-diffusion indicator, which is now used throughout the paper:

$$\tilde{\gamma} = \frac{\log\left(\sum_{\boldsymbol{i},|\boldsymbol{i}|\neq 0} \kappa_{\boldsymbol{i}} \, |\boldsymbol{c}_{\boldsymbol{i}}(t)|^2 + (\boldsymbol{c}_0 - \boldsymbol{x}_{td})^2 + 1\right)}{\log t} \tag{22}$$

It is worth highlighting a few properties of the indicator in Eq. (22):

1) As other dynamic indicators, $\tilde{\gamma}$ captures in a single scalar the evolution of a vector field and thus can be used to build a cartography (or a qualitative map) of the dynamic evolution of the system for different initial conditions.

2) The indicator is directly computed from the NCI model without any added computational cost.

3) The indicator contains information on the mean and variance of the ensemble. If the mean and variance are bounded, the indicator goes asymptotically to zero, in which case the dynamics is asymptotically insensitive to the uncertainty.

IV. Surface Motion

The motion of the spacecraft during touchdown and the phase after landing where it can bounce and move around the surface is mainly defined by the shape of the surface, the characteristics of the surface material to dissipate the energy of the spacecraft, and the presence of surface features like rocks and/or craters. Various previous works have looked into the problem of dynamically modeling the motion across the surface of an asteroid. For the Hayabusa mission, an initial analysis for the deployment of a target marker on the surface of Itokawa was performed in [15]. For this initial analysis, a point mass model of the lander with an energy damping factor in the normal velocity, called the coefficient of restitution (CoR), was used. A minimum height from the asteroid surface was chosen for which the simulation would stop if it was not reached after the last bounce, fixing the settling location. This model was expanded upon in [45], where a spherical mass was considered, introducing a friction and rolling resistance parameter. In [16], a parametric sensitivity study was performed for this model, showing that the CoR is much more important than the absolute value of the friction and rolling resistance with regards to the settling time and location of the lander. Other important parameters found for successful landing are the deployment velocity magnitude and direction, and the mass distribution of the lander. Similar conclusions were drawn in the tracking of the deployment of spherical markers for the Hayabusa 2 mission in [46]. A more complex nonspherical shape bouncing model was then developed in [17], using the Stronge method. This method uses an energetic version of the CoR, together with separating different types of behavior during contact like slip and stick. This model was investigated both numerically [47] and experimentally [48], showing that the friction is more important in this case but the deployment conditions and CoR still dominated the outcome of the landing, further verified for Hayabusa 2 rover deployment studies [49]. All of the previously mentioned studies consider the so-called hard surface model, which assumes that the local surface at impact is always a single large monolithic structure larger than the lander. If, on the other hand, a soft-surface model is necessary where the surface consists of a large set of small particles, i.e., regolith, discrete element methods (DEMs) are needed to determine the response of the lander's motion to the surface. In [50], this analysis was performed for the Phobos surface, and it was found that using a DEM model a relation between impact geometry and the hard-surface parameters like CoR and friction can be found such that the hard-surface model can still be used for larger scale simulations if these properties become a function of impact angle and velocity, removing the computational burden of DEM simulations.

In this work, the main goal is to present a novel method for analyzing the motion across the surface of an asteroid and design a robust trajectory that has a high probability of settling on the surface of the asteroid under large uncertainties. This is especially relevant for an initial analysis of the landing maneuver, where surface properties like the local slope, rock sizes and distribution, and surface composition will only be known with a high degree of uncertainty. But even after rendezvous with the target body and in-depth remote investigations, the surface mechanical properties will still be highly uncertain. Thus, presenting and validating the ability of the NCI and pseudo-diffusion indicator-based method to incorporate uncertainties is the main focus of this work, for which a low- to medium-fidelity surface motion model is favorable as it allows to better present the general capabilities of this method without introducing complex dynamic behavior from the contact model and requiring case-specific information. It is noted that the sparse sampling method of the NCI allows for increasing the amount of uncertain parameters without significantly increasing the computational time. Therefore, higher-fidelity models with a larger parameter space do not have any inherent properties that limit their use within the framework presented here.

A. Surface Impact

The spacecraft is assumed here to be a point mass, while Dimorphos is modeled as a triaxial ellipsoid. Therefore, Dimorphos can be parameterized using the previously defined ellipsoidal axes of Table 1 as follows:

$$E(x,y,z) = \frac{x^2}{a^2} + \frac{y^2}{b^2} + \frac{z^2}{c^2} = 1 \tag{23}$$

where the x, y, and z coordinates are with respect to the ellipsoid center. This significantly simplifies the condition of when an impact occurs to

$$E(x,y,z) \leq 1 \tag{24}$$

and the normal at any point along the surface can be found through the gradient operator:

$$\hat{\boldsymbol{n}}(x,y,z) = \nabla E(x,y,z) = 2\left[x/a^2, y/b^2, z/c^2\right]^T \tag{25}$$

The surface of a small body can often be modeled as either a hard-rock-type surface or a soft-regolith-type surface [50]. During its multiple impacts, Philae encountered both of these types of surfaces [51], showing the importance of both of these types of models. For the soft surface case, a numerically expensive DEM is usually used, which also requires a good knowledge of the surface conditions and parameters. Hence, it is less useful for this type of analysis.

The energy dissipation during an impact is characterized using the CoR $0 \leq \epsilon \leq 1$, which is defined here as follows:

$$\epsilon = \frac{v_N^+}{v_N^-} \tag{26}$$

where the plus and minus signs indicate the post- and pre-impact velocity, respectively, and the N subscript represents the normal component of the vector. Using the geometry of the impact shown in Fig. 2a, the postimpact velocity vector can be calculated as follows:

$$\boldsymbol{v}^+ = \boldsymbol{v}_T^+ + \boldsymbol{v}_N^+ \tag{27}$$

$$\boldsymbol{v}_N^+ = -\epsilon(\hat{\boldsymbol{n}} \cdot \boldsymbol{v}^-)\hat{\boldsymbol{n}} \tag{28}$$

$$\boldsymbol{v}_T^+ = \boldsymbol{v}^- - (\hat{\boldsymbol{n}} \cdot \boldsymbol{v}^-)\hat{\boldsymbol{n}} \tag{29}$$

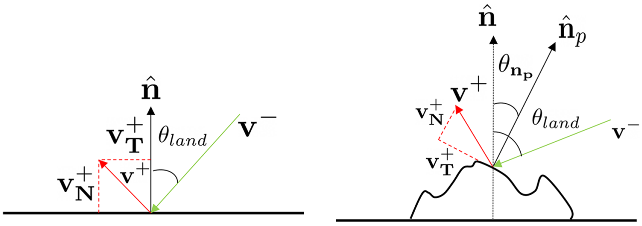

a) No surface features **b) With surface features**

Fig. 2 Two-dimensional representation of the geometry during landing.

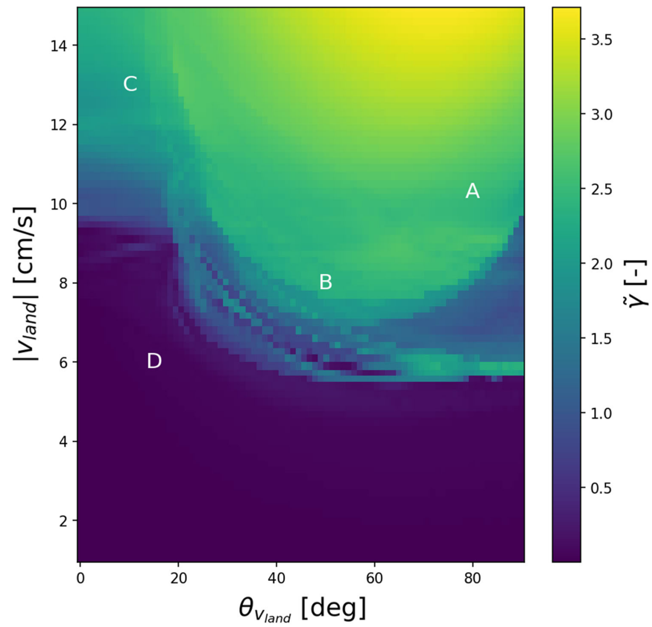

Fig. 3 The $\tilde{\gamma}$ map of the NCI model at DART crater location.

Thus, given an impact point and impact velocity, the postimpact velocity can be calculated and used to initialize the following arc of ballistic flight that is propagated using the dynamics described in Sec. II. As the analysis here is mainly concerned with finding the conditions for settling on the surface and less with the exact settling location, only the CoR is considered to simplify the analysis, and no tangential friction is implemented. This can result in the tangential velocity remaining high whereas the normal velocity goes toward zero, keeping the kinetic energy always above zero. To solve this, a procedure similar to [45] is followed, where if the normal velocity is below a minimum value, the bouncing is determined to have stopped. After tuning for minimal difference between settling locations for different values, the minimum normal velocity was chosen to be 0.5 cm/s.

For the design of landing trajectories, it is important to study which landing conditions lead to the highest probability of a successful landing, which is defined as having the spacecraft remain on the surface of Dimorphos. In this case, the important uncertain dynamic parameters that govern this probability are ϵ and the uncertainties in the gravitational field given here by the spherical harmonic coefficients. To find the range of landing conditions that give a high probability of success, a large number of landing velocities $|\boldsymbol{v}_{\text{land}}|$ and landing angles θ_{land} (defined as the angle between the local normal and the incoming velocity vector; see Fig. 2a) are taken and used to calculate the initial postimpact velocity vector. From there, based on the sampling method discussed in Sec. III.A, a set of samples is propagated. Each time if one sample is determined to impact with Dimorphos, the postimpact vector is calculated again. Once enough time has passed (defined here to be 12 h), the pseudo-diffusion indicator is calculated. From various previous studies, the range of possible values for ϵ is taken to be [0.55, 0.85] (see, e.g., [52–56]). Furthermore, to also include uncertainties during ballistic flight, the C_{20} and C_{22} (thus impacting the fourth-degree coefficients as well) are taken to be in the range of their nominal value with 10% uncertainty, which is close to the uncertainties given for most parameters in the Didymos reference model [26]. For all results discussed in the rest of the paper, these uncertainties are kept constant. Only when the rock model is discussed in Sec. IV.B will another uncertainty be added, with the CoR and spherical harmonic coefficient remaining the same. For the CoR and spherical harmonic uncertainties, the results of $\tilde{\gamma}$ are shown in the map in Fig. 3.

As is explained in Sec. III.B, low $\tilde{\gamma}$ indicates regions of low diffusion, i.e., where trajectories that have slightly different initial conditions or dynamic parameters still behave similarly and stay close to each other. In the case of a spacecraft landing scenario, the lowest diffusion happens when all realizations of the uncertainties result in the spacecraft remaining on the surface of Dimorphos. When part or all of the realizations result in the spacecraft bouncing away from the surface into prolonged ballistic flight, the diffusion increases as during the ballistic flight the trajectories move away from each other due to the nonlinear dynamics. Therefore, the regions of low $\tilde{\gamma}$ correspond to landing conditions that allow the spacecraft landing on Dimorphos with a high likelihood, which is defined here as a successful landing condition. It can be seen that this happens for most conditions with the $|\boldsymbol{v}_{\text{land}}| < 10$ cm/s and $\theta_{\text{land}} < 20$ deg. The calculated escape velocity of Dimorphos, which is around 0.09 cm/s [57], is close to the limiting velocity here, considering also energy damping due to the first bounce. As the landing velocity decreases until around 6 cm/s, successful landings become more likely for higher θ_{land}. After that, the direction of impact does not have any significant impact on the $\tilde{\gamma}$ value. This corresponds to the closing of the zero velocity curves around the L_1 and L_2 points [13], thus not allowing for transportation outside the region of Dimorphos regardless of the impact angle. For most of the landing velocities above 10 cm/s, $\tilde{\gamma}$ is much higher, and thus there is a low likelihood of having a successful landing. The transition region between these two limits (i.e., the region between 5 and 10 cm/s for larger impact angles) shows many interesting structures, which result in part of the trajectories landing on Dimorphos and part of them going into bounded motion around both the primary and secondary.

Figure 4a shows the probability of a successful landing, generated by sampling the NCI model 500 times and measuring the number of points that remain on the surface of Dimorphos. When comparing to the $\tilde{\gamma}$ of Fig. 3, it can be seen that a high landing probability corresponds to a low value of $\tilde{\gamma}$. One region, around 8–9 cm/s of landing velocity and 0 deg impact angle, has a low landing probability, which is not immediately clear in the $\tilde{\gamma}$ map of Fig. 4a. However, this can also be shown to exist when the map is focused to lower $\tilde{\gamma}$ values by taking all $\tilde{\gamma} > 1.5$ and fixing them to a value of 1.5, as is done in Fig. 4b. More details can now be seen in certain regions, showing a similar structure as seen for the probability map around 8–9 cm/s. Thus, this verifies the function of the $\tilde{\gamma}$ indicator in finding initial conditions that remain close to the touchdown location.

To show the relationship between the value of $\tilde{\gamma}$ and the evolution of an ensemble of trajectories at a given time after touchdown, 500 realizations of the uncertain parameters were propagated (using the true dynamic model, not the NCI polynomial model) forward for 12 h from four touchdown conditions from the regions designated with the letters A, B, C, and D in Fig. 3. The resulting trajectories, plotted in the synodic reference frame in all three dimensions, are illustrated in Fig. 5. The final positions of all the sample trajectories can also be seen in Fig. 6. The two cases in the transition region, A and B, have part of the trajectories that landed on Dimorphos and part remaining in a bounded region around the asteroid system. For case C, with high $\tilde{\gamma}$, it can be clearly seen that all samples escape from the surface of Dimorphos and move away from both bodies. Whereas for D, with low $\tilde{\gamma}$, all trajectories remain on the surface of Dimorphos, some bouncing several times before going stationary. From the landing probability and clamped $\tilde{\gamma}$ map in Fig. 4, three other regions of interest, denoted by E, F, and G, are investigated using the same setup, which can be seen in Figs. 5e–5g and 7. Case E has a relatively higher $\tilde{\gamma}$ than the surrounding area. As can be seen in Fig. 5e, this is due to the fact that there are trajectories landing on Dimorphos, trajectories going into far circumbinary orbits, and also trajectories

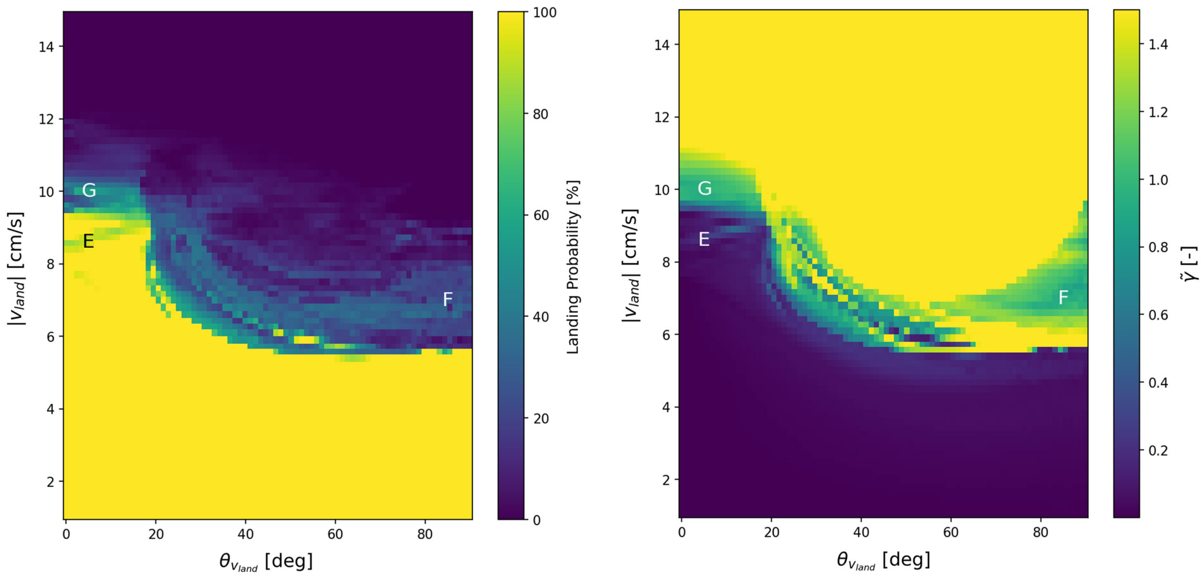

a) Landing probability

b) Clamped $\tilde{\gamma}$ map

Fig. 4 Map for the probability of landing calculated from the NCI model and $\tilde{\gamma}$ map with only lower values shown.

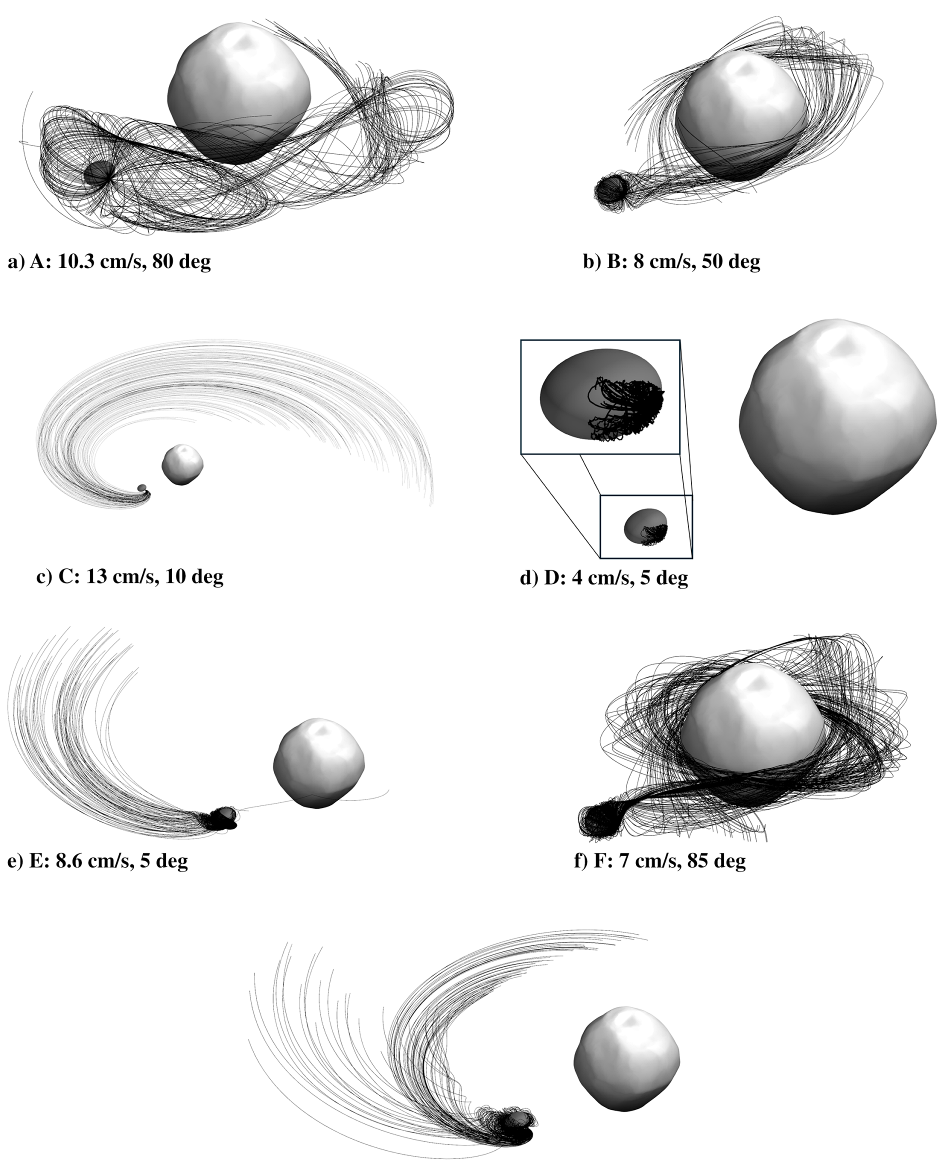

a) A: 10.3 cm/s, 80 deg

b) B: 8 cm/s, 50 deg

c) C: 13 cm/s, 10 deg

d) D: 4 cm/s, 5 deg

e) E: 8.6 cm/s, 5 deg

f) F: 7 cm/s, 85 deg

g) G: 10.0 cm/s, 5 deg

Fig. 5 Sets of trajectories plotted from the example MC analyses.

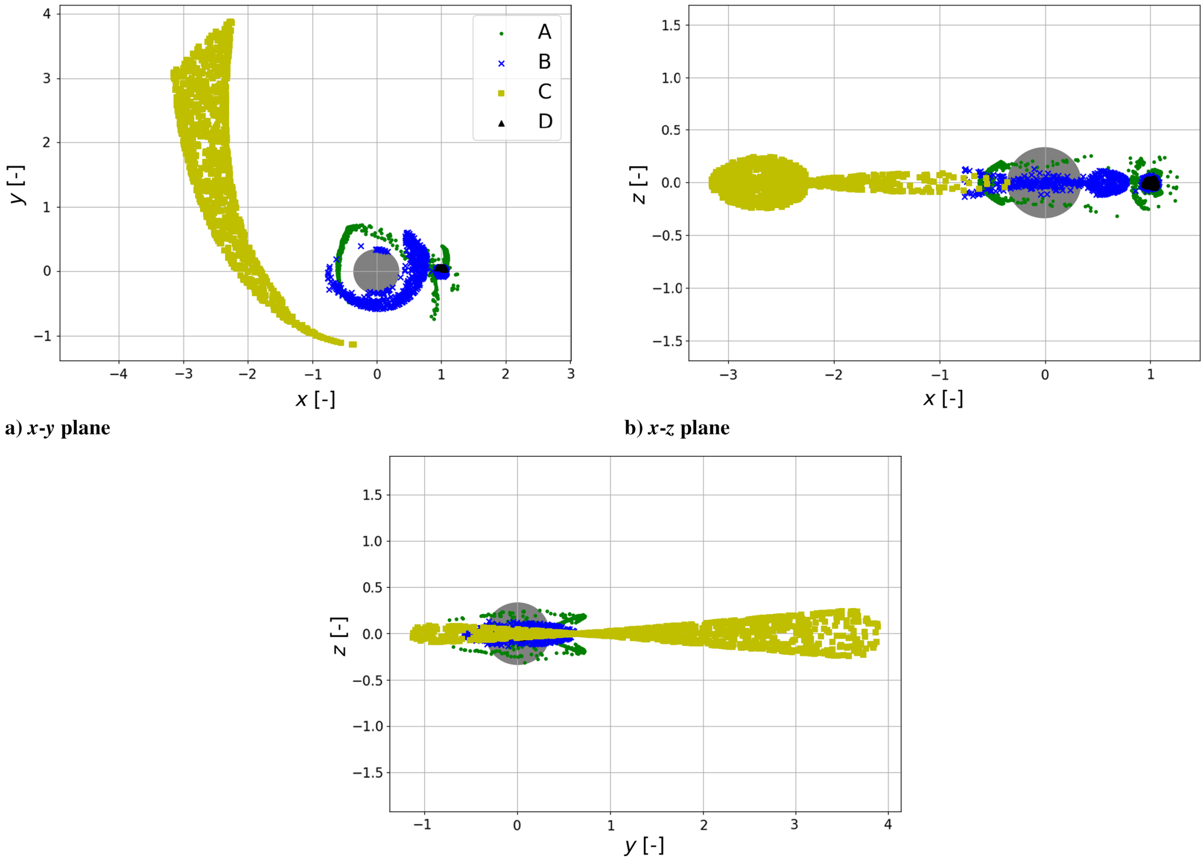

a) *x-y* plane

b) *x-z* plane

c) *y-z* plane

Fig. 6 Distribution of the final locations of the MC analyses.

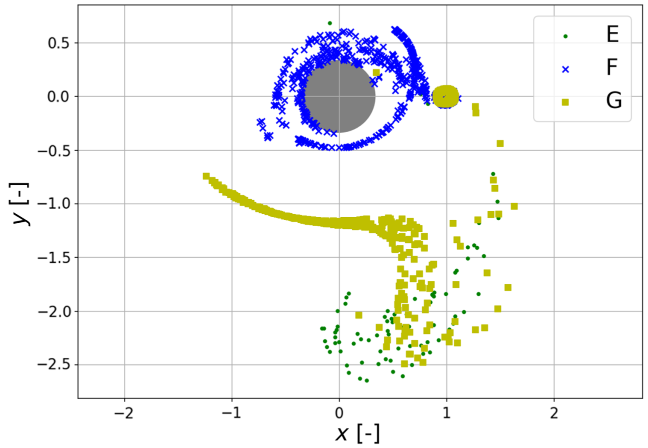

Fig. 7 Distribution of the final locations of the MC analyses from Figs. 4a and 4b.

landing on Didymos. Case F is located in a region with a high impact angle but low $\tilde{\gamma}$ compared to the surrounding values. In Fig. 5f, some of the trajectories can be seen to bounce directly from Dimorphos to Didymos, and impact on Didymos. Compare this to case B in Fig. 5b, which has a similar velocity but lower impact angle, and it can be seen that part of the trajectories of B go into larger orbits around the primary instead of impacting on its surface. Thus the general $\tilde{\gamma}$ value of F is relatively low, while the Dimorphos landing probability also remains low. Case G is also of interest, as even though the landing probability is relatively high, the $\tilde{\gamma}$ value is also high. As mentioned before, the calculated escape velocity of Dimorphos is roughly 0.09 cm/s, which is close to the velocity of region G. Thus, it can be seen that if a large amount of sample from the CoR and SH coefficients uncertainty distribution is taken around this velocity, several different dynamic effects can be observed. A relatively large amount of trajectories will remain on the surface, whereas there will also be a significant amount of trajectories bouncing and escaping the system with just enough energy, as can be seen in Fig. 5g.

B. Surface Rocks

In the previous section, the only parameter that influences the postimpact bounce velocity is the CoR ϵ, where the normal vector is calculated assuming a smooth ellipsoid as the shape of Dimorphos. This does not necessarily correspond to the real global shape of Dimorphos, or most small bodies in the solar system in general. For a significant amount of the small bodies that have their surfaces imaged, several different types of surfaces were present across the body [47]. At bodies like Eros [58], Itokawa [52], and 67p [51], both smooth and rocky regions were found. Therefore, besides the smooth surface model, the influence of rocks and boulders needs to be implemented to ensure proper modeling of the surface motion of the lander.

A stochastic model for the effects of rocks was introduced in [45], in which a probability was associated with the chance of colliding with a rock, and then another probability was associated with how much the local normal vector is changed due to the presence of a rock on the surface. These probabilities were estimated using a large number of simulations with persistent rocks placed on the surface. In [16], it was argued that a stochastic rock model would bias the lander toward low-slope regions as it cannot get stuck on boulders located in high-slope regions, and, furthermore, grazing impacts with rocks would not be registered. Other studies like [18,19] used persistent rock models as well to increase the fidelity of the model.

In this work, the main focus is on the effect of the uncertain landing conditions, including uncertainty in the local surface features, on the motion of the spacecraft. Therefore, the use of accurate shape models is not as beneficial, and models that more easily incorporate the uncertain nature of the problem are preferred. Therefore, the rocks are modeled here as a stochastic perturbation on the normal vector $\hat{\boldsymbol{n}}$, used in Eqs. (28) and (29). The model considered here is thus not only uncertain in terms of the parameters of the dynamic model but now also stochastic due to the "noisy" normal vector.

In contrast to the stochastic model described in [45], the model used here considers that at every contact with the surface, the normal vector is altered according to the rock model. Physically, this means that there is no smooth area on the asteroid surface. As mentioned before, most small-body surfaces are a combination of smooth and rocky regions, which requires adding a second random variable that models the chance of impacting a rock, adding complexity to the model. Even though this would be necessary for some asteroid surfaces, the simpler model considered here investigates two extreme cases, which thus shows that the methodology developed in this paper would work as well for a model considering a mixed smooth and rocky surface. Another difference from the previously defined stochastic rock model is that in this work the distribution of the normal is based upon the investigation of rock shapes encountered in previous asteroids missions. For example, it was found that when the boulders from images of the Hayabusa 2 spacecraft are fitted to ellipsoidal shapes, the mean values of b/a and c/a were found to be around 0.7 and 0.44, respectively [59]. This can then be converted to a distribution of normal angles $\theta_{\hat{\boldsymbol{n}}_p}$ and azimuth angles $\phi_{\hat{\boldsymbol{n}}_p}$ of the perturbed normal vector $\hat{\boldsymbol{n}}_p$ w.r.t. $\hat{\boldsymbol{n}}$, where the different variables are explained graphically in Fig. 2b ($\phi_{\hat{\boldsymbol{n}}_p}$ is defined as the rotation around the $\hat{\boldsymbol{n}}$ and thus not shown in the 2D figure). For example, the found distribution for $\theta_{\hat{\boldsymbol{n}}_p}$ is shown in Fig. 8a. This distribution is then fitted to a beta probability distribution function and implemented in the dynamic model. To determine the influence of different shapes, a more flat-shaped rock ($b/a = 0.9$ and $c/a = 0.2$) was implemented as well, as shown in Fig. 8b. These two different rock shapes are hereby referred to rock shapes A and B, respectively. If increased fidelity is needed, the same procedure can be used to combine various different rock shapes to create a single distribution of normal angles. However, for a first analysis, here a single rock shape is used for each simulation.

The $\tilde{\gamma}$ map of the new dynamic system with the distribution taken from both rock shape set A (left) and rock shape set B (right) can be found in Fig. 9. First, it can be seen that the difference between the two rock distributions is minimal, thus showing that the shape of the rocks has less of an effect on the large-scale distribution of the final states. If compared with the results without rocks, the main difference is that the impact angle has less impact on the results than that of the landing velocity. It can be seen that now the main driver is that the landing velocity should be below around 6 cm/s to ensure a high probability of landing. The impact angle should still be low, as there still is a slight slope on the boundary between the low and higher diffusion areas, but this slope is much less significant compared to Fig. 3.

Three different example MC analyses are performed in a similar manner to before to analyze these different regions, where each one is taken with a similar impact angle but landing velocity taken from the

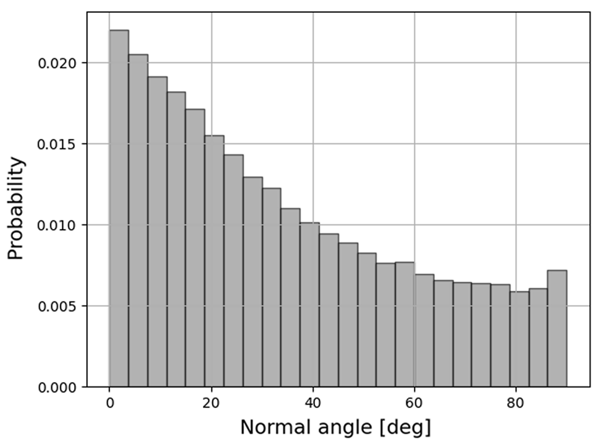

a) Rock shape A

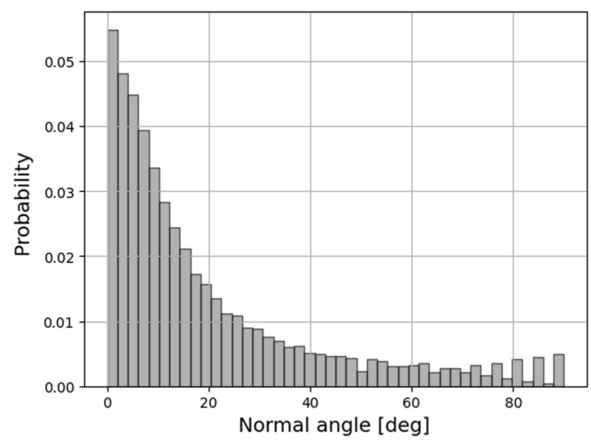

b) Rock shape B

Fig. 8 Distribution of θ_{n_p} for different rock shapes.

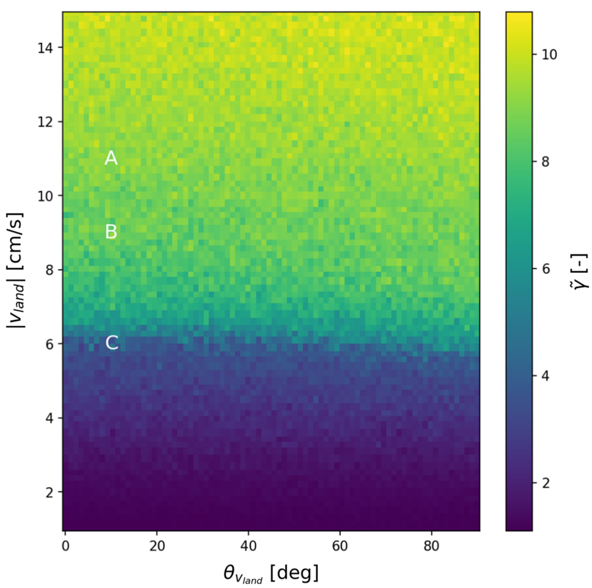

a) Rock shape A

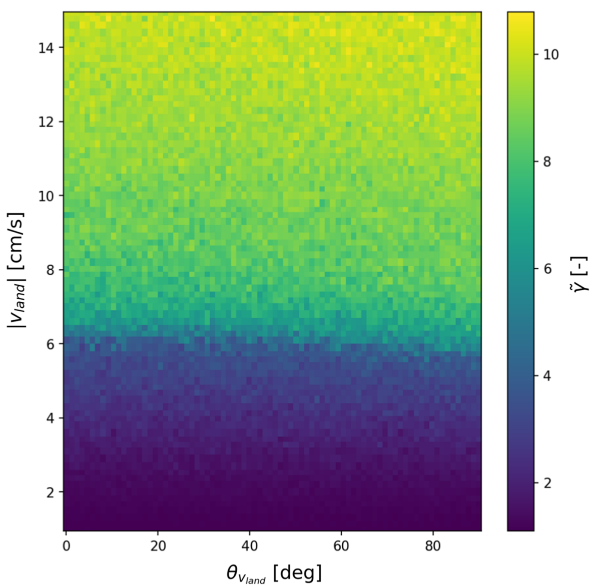

b) Rock shape B

Fig. 9 The $\tilde{\gamma}$ maps for different rock distributions at DART crater location.

different regions discussed before. The results can be seen in Figs. 10 and 11. As expected, C shows that most of the trajectories remain bounded on the surface of Dimorphos. The difference between A and B is less prominent in terms of $\tilde{\gamma}$ values, as for these regions the diffusion from the desired touchdown regions is in general quite large. However, if the original definition of the diffusion indicator $\tilde{\gamma}_o$ from Eq. (18) is applied instead of the diffusion indicator based on the touchdown location, $\tilde{\gamma}$, different regions can be observed, which are shown in Fig. 12. For velocities between 8 and 10 cm/s, the diffusion is high as a significant amount of trajectories move from Dimorphos to Didymos, settling on the surface of Didymos. Furthermore, there are also several trajectories moving outward of the

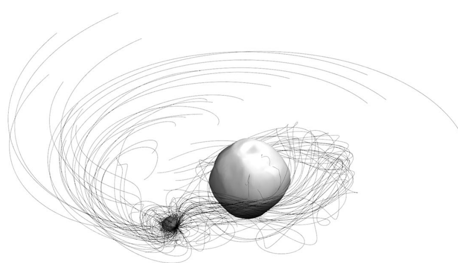

a) A: 11 cm/s, 10 deg

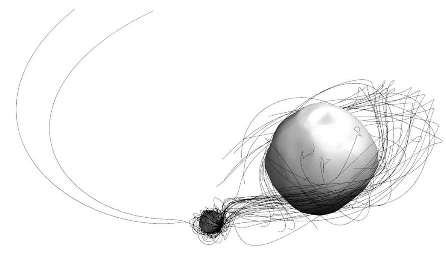

b) B: 9 cm/s, 10 deg

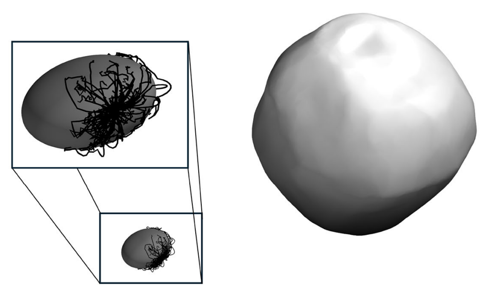

c) C: 6 cm/s, 10 deg

Fig. 10 Trajectories plotted from the example MC analyses, including the stochastic rock model.

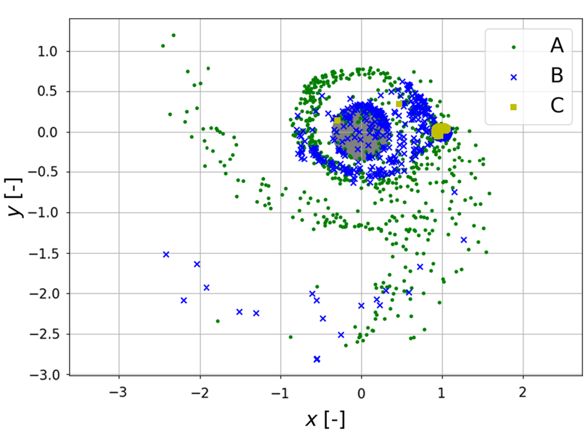

a) *x-y* plane

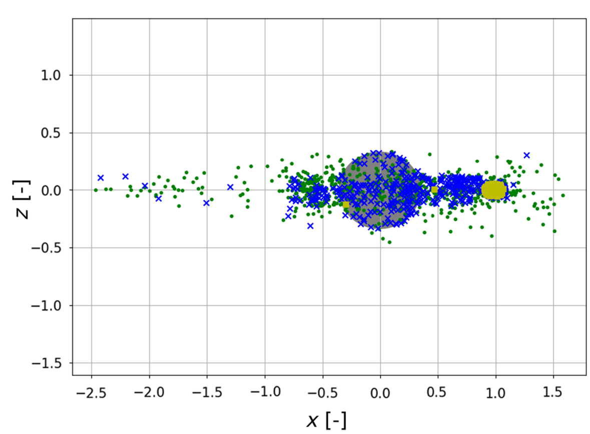

b) *x-z* plane

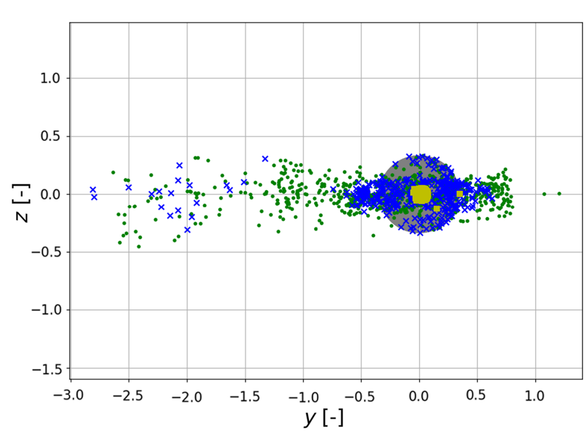

c) *y-z* plane

Fig. 11 Distribution of final locations of the MC analyses, including the stochastic rock model.

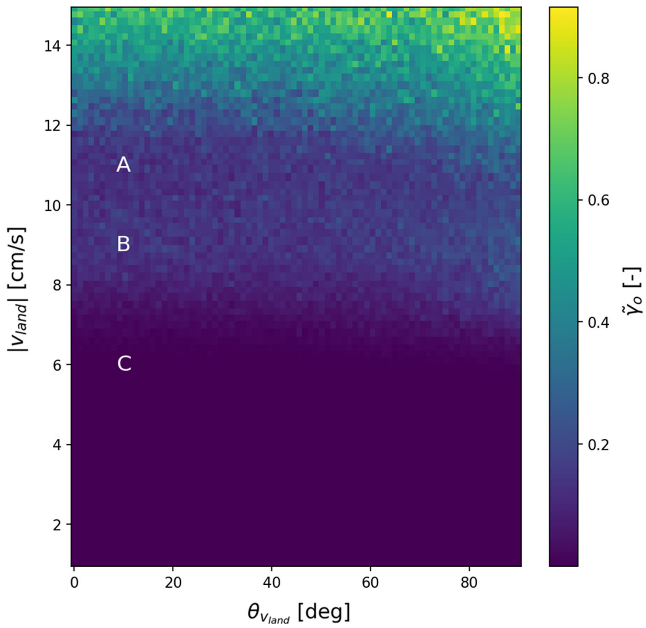

Fig. 12 Map for rock set A at DART crater location, using the $\tilde{\gamma}_o$ definition in Eq. (18).

system, which causes a generally high diffusion as trajectories stemming from these initial conditions can go into three different regions: settling on Dimorphos, settling on Didymos, and escaping the system. For initial conditions with a velocity higher than 10 cm/s, less transport to the surface of Didymos is occurring, and more are escaping the system, causing the general diffusion to be less high than for region B, even though more trajectories escape the system. This is important when considering, for example, the transport of natural ejecta from the DART impact re-impacting the surface. However, when considering a spacecraft landing trajectory, the novel definition for $\tilde{\gamma}$ of Eq. (22) is preferable as it only takes into account the diffusion from the desired touchdown location.

V. Minimum Touchdown Velocity

During the proximity operations at Didymos, the spacecraft will move slowly toward the bodies over time. During the final phase, when it is the closest to the system, the maneuver to put it on the landing trajectory toward Dimorphos will be executed. As mentioned before, for this study it is assumed that the translational state is not continuously controlled during descent. Hence, the minimum possible landing velocity cannot be controlled and is determined by the natural dynamics of the system.

This minimum landing velocity for Dimorphos is determined as follows: For the nominal case, the authors of Ref. [60] developed a bisection method to determine the minimum touchdown velocity for ballistic landings on asteroid surfaces. This was then further extended in [14] to use uncertainty propagation methods to include state and dynamic uncertainties in the process. This method is used here to determine the touchdown velocity, considering the current, pre-arrival uncertainties in the total mass of the system and the mass distribution of Dimorphos. For the sake of completeness, this method is explained here as well.

The method starts by selecting a landing location and initializing an upper and lower bound for the landing velocity, v_l and v_u, respectively. For each iteration of the algorithm, the landing velocity v_c is taken to be the middle point of these bounds, i.e., $v_c = (v_u + v_l)/2$. As was shown in Sec. IV, the highest probability of the spacecraft remaining on the surface of Dimorphos after bouncing is when the landing happens perpendicular to the surface. Therefore, the impact angle is taken to be 0 deg, and the landing state can be seen as a point located at the desired landing location with the velocity vector pointing toward the center of Dimorphos. The trajectory is then propagated backward in time until either the spacecraft reaches a

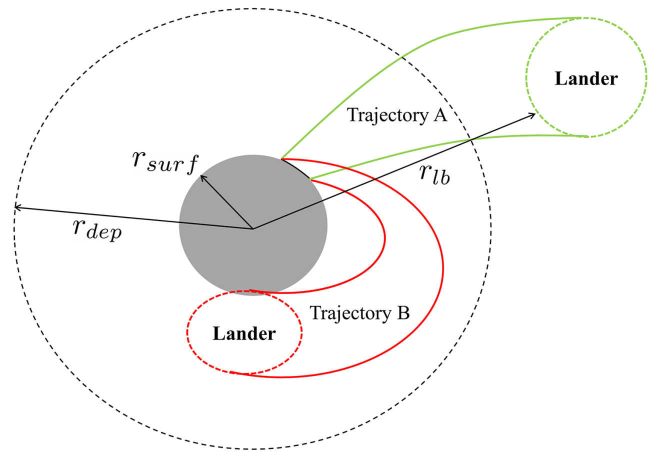

Fig. 13 Definition of the variables and two different cases for the bisection method.

predetermined deployment distance r_{dep} (which can be either the distance at which a mothercraft is orbiting at deployment or the previous operational orbit of the spacecraft before starting the landing maneuver), the spacecraft lands back on Dimorphos, or the flight time of 12 h is reached. If r_{dep} is reached, the landing velocity might be too large, and thus the upper bound of the next iteration is lowered to the v_c of the current iteration. For the other possibilities (flight time larger than 12 h or re-impact on the surface), v_c is too low, and thus the lower bound of the landing velocity for the next iteration is set to v_c of the current iteration. A maximum flight time of 12 h is selected for operational purposes and to minimize the maximal growth of the set of states. This process is repeated until the difference between v_l and v_u reaches a set tolerance, taken here to be $1 \cdot 10^{-8}$.

In the case that uncertainties are also considered, the process remains relatively similar except for the fact that the state is now an uncertain set, which needs to be propagated using the NCI method discussed in Sec. III.A. Furthermore, determining how to adjust the velocity bounds is now done according to the value of the minimum distance between the set of lander states and Dimorphos. The method is shown graphically in Fig. 13, where case A shows the scenario where the full set of lander states reaches the deployment distance and in case B, the landing velocity is not high enough to reach the deployment distance. Additionally, a summary of the method is shown in Algorithm 1.

Figure 14 shows the results for Dimorphos, with $r_{\text{dep}} = 2.0$ km (the final orbital distance of Juventas) and the uncertainties at 10% of their nominal values. The surface of Dimorphos can be divided into two different regions, the side facing away from Didymos (longitude between −90 and 90 deg) and the side facing toward Didymos (longitude between −90 and −180 deg and between 90 and

Algorithm 1: Minimum touchdown velocity algorithm

Set v_{lb}, v_{ub}
Set $\mu_p \pm \sigma_{\mu_p}, \mu_s \pm \sigma_{\mu_s}$
Set $C_{20,s} \pm \sigma_{C_{20,s}}, C_{22,s} \pm \sigma_{C_{22,s}}$
while $|v_{ub} - v_{lb}| < TOL$ **do**
  $v_l = (v_{ub} + v_{lb})/2$
  Propagate $\tilde{\Omega}_{x_f} \rightarrow \tilde{\Omega}_{x_0}$
  if $r_{lb} < r_{\text{surf}}$ **then**
    $v_{lb} = v_l$
  else if $r_{lb} > r_{\text{dep}}$ **then**
    $v_{ub} = v_l$
  else
    $v_{lb} = v_l$
  end if
end while

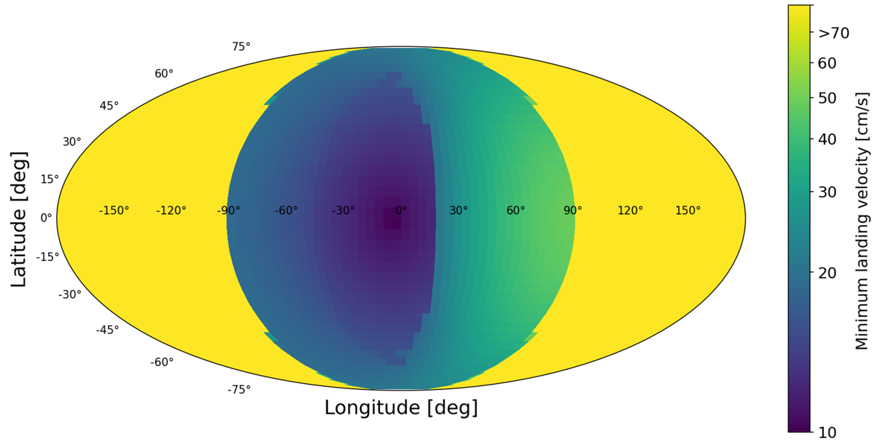

Fig. 14 Minimum landing velocities for different areas, plotted with a power law distribution.

180 deg). The latter region shows in general high landing velocities as it needs to travel further to reach the deployment distance and to avoid Didymos. Only at high latitudes can lower touchdown velocities be reached, as Didymos can be avoided more easily from these landing locations. In general, the landing velocities in this region are too high to be feasible for a ballistic landing strategy. For the region facing away from Didymos, the lowest touchdown velocities are near the (0, 0) deg latitude and longitude point, where velocities around 5 cm/s can be found. Moving toward the desired landing location at the DART crater [i.e., (0, 90) deg latitude and longitude], the velocity increases again, reaching around 38 cm/s. As determined in Sec. IV, this landing velocity does not guarantee that the spacecraft remains on the surface of Dimorphos after touchdown (for both the cases of rocks and no rocks). Therefore, either the assumption of landing perpendicular to the surface needs to be relaxed or a braking maneuver needs to be added to the landing trajectory to reduce the speed of the spacecraft before touchdown.

Figure 15 shows the influence of the incoming velocity direction on the minimum landing velocity. The angle $\theta_{v_{\mathrm{land}}}$ corresponds to the impact angle discussed in Sec. IV, and the azimuth is the angle of the landing velocity vector with respect to the negative x axis of the synodic frame. As can be seen from Fig. 15, there are options for lower velocity landings (for settling requiring between 7 and 10 cm/s) with a very shallow impact angle around 180 deg azimuth, corresponding to the velocity vector pointing away from the barycenter of the system. However, even for the lower velocities found there, the very shallow impact angle will significantly increase the likelihood of the spacecraft bouncing away from the surface again, as was shown in Sec. IV. Therefore, if the goal is to land in or near the DART impact crater, a braking maneuver closer to the surface is the only option to have a high probability of a successful landing.

VI. Robust Trajectory Optimization

After finding the target conditions of the lander at the surface in Sec. IV, the goal now is to design a trajectory that can ensure that the spacecraft can reach these conditions reliably. As mentioned in Sec. V, the minimum touchdown velocity at the DART crater for a direct deployment from $r_{\mathrm{dep}} = 2.0$ km is around 38 cm/s, whereas from the $\tilde{\gamma}$ maps of Sec. IV it was found that the touchdown velocity should be below 10 cm/s, preferably below 7 cm/s if a rocky environment is found, to ensure a high probability of settling on the surface of Dimorphos. Therefore, a braking maneuver is needed between the deployment maneuver and the time of landing.

For the ballistic landing considered here, there is no dedicated navigation system that is capable of estimating the state and correcting for off-nominal conditions; hence, the braking maneuver is performed open-loop using a precalculated ΔV maneuver. As the spacecraft has no capabilities to correct for the uncertainties in the state of the spacecraft stemming from maneuver errors and dynamic model uncertainties, both the deployment and braking maneuvers need to be generated such that the landing success percentage is the highest. Normally, this is done by first designing a nominal trajectory, then doing a sensitivity analysis (often using an MC method) to assess the impact of uncertainties, and finally altering the nominal trajectory based on the found sensitivities. This process often needs multiple iterations and is thus time-consuming and can result in worse trajectories with added safety margins [22]. In this section, the NCI uncertainty propagation technique is used to generate landing trajectories that directly take into account all the different uncertainties and minimize its sensitivity to them.

The approach taken here is based on the direct multiple shooting method developed in [61]. The landing trajectory is divided into two

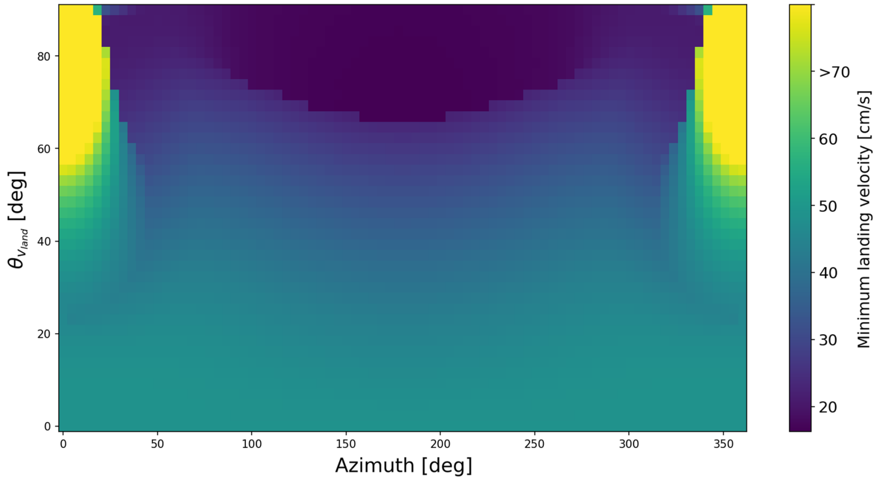

Fig. 15 Minimum landing velocity for different landing vector orientations at the DART crater.

segments: the deployment segment spanning from the deployment point to the braking point, and the terminal segment stemming from the braking point to the landing point. A nonlinear programming (NLP) solver is then used to find the optimal values of the decision variables $\boldsymbol{u}$, which consist of the deployment velocity vector $\boldsymbol{v}_{\text{dep}}$, the braking maneuver $\Delta\boldsymbol{v}$, and the time of the braking maneuver $t_{\Delta v}$. The trajectory is then propagated using the selected $\boldsymbol{u}$ after which the different objectives and constraints are evaluated and used to select a new $\boldsymbol{u}$. When considering uncertainties, this pointwise propagation of the state is substituted by the propagation of the uncertainty set, which is performed here using the NCI method. In principle, the full trajectory can be propagated in one go, obtaining one polynomial representation of the landing trajectory under uncertainty. However, both the required polynomial degree and number of samples increase quickly as the number of uncertain variables increases. Therefore, it is more efficient to separate the polynomial for the two different segments. The continuity between the two segments is guaranteed using a re-initialization approach, which is shown graphically in Fig. 16. First, the uncertainty set at the deployment point is propagated using NCI to the braking point, shown as the gray areas in the left side of Fig. 16. The initial uncertainty range for the terminal segment needs to be represented by an upper and lower bound of the various state variables, i.e., a hypercube in phase space. This means that the shape of the final set of states at the braking point, which is often shaped very differently from a hypercube, cannot be used directly as an input for the initial state uncertainties of the terminal phase. Hence, the uncertainty set at the braking point is re-initialized as a hypercube that conservatively bounds the set (the dashed box). This hypercube can be used as the input for the following phase and is then propagated through the terminal segment until the time of landing. As the resulting hypercube is an overestimation of the actual uncertainty set, a set of samples is first propagated using the deployment segment polynomial and then used as an input for the terminal segment polynomial to obtain the actual distribution at the landing point (see Fig. 16). This distribution is then used to obtain the necessary objective and constraint values that are formulated as part of the NLP, which are now functions of the distribution of landing trajectories.

The robust optimization problem considered here is formulated as follows:

$$\min_{\boldsymbol{u}} \quad \max(\mathrm{diag}(\Sigma_{r,\text{land}})) \tag{30}$$

$$\text{s.t.} \quad \boldsymbol{x}_{k+1} = \tilde{\Omega}_{t_{k+1}}(\boldsymbol{\xi}_k), k = 0, 1 \tag{31}$$

$$\mathbb{E}[\boldsymbol{r}_{\text{land}}] - \boldsymbol{r}_{\text{crater}} < 100 \text{ m} \tag{32}$$

$$\mathbb{E}[|\boldsymbol{v}_{\text{land}}|] < 8 \text{ cm/s} \tag{33}$$

The maximum variance of the state at the final time is selected as the cost function that needs to be minimized. Using this objective will desensitize the landing trajectory to the uncertainties and thus reduce the landing footprint. To ensure that the spacecraft will land mostly in the DART crater hemisphere, constraint (32) is added to ensure that the mean landing state should be within 100 m of the DART crater location. Constraint (33) is derived from the $\tilde{\gamma}$ maps, where landings below this value have sufficiently low $\tilde{\gamma}$ such that the probability of settling on the surface is high. For the rocky case, the θ_{land} constraint can be relaxed, whereas the $|\boldsymbol{v}_{\text{land}}|$ constraint needs to be lowered to 7 cm/s. However, it will be shown that the result with the constraints set for the smooth surface case also works well for the rocky case, and thus this setup is kept for now.

Table 3 Results of the optimization of the landing trajectory

Variable	Point	Robust
v_{dep}	40.9 cm/s	20.8 cm/s
ϕ_{dep}	186.3°	223.0°
θ_{dep}	93.7°	88.6°
Δv	39.9 cm/s	7.2 cm/s
$\phi_{\Delta v}$	185.3°	165.18°
$\theta_{\Delta v}$	84.7°	87.1°
$t_{\Delta v}$	7.071 h	7.703 h
Landing success	74.3 %	99.8 %
Landing latitude (mean, $1-\sigma$)	$2.49 \pm 26.5°$	$18.72 \pm 13.5°$
Landing longitude (mean, $1-\sigma$)	$77.9 \pm 41.5°$	$5.9 \pm 22.8°$
θ_{land} (mean, $1-\sigma$)	$35.9 \pm 19.4°$	$37.9 \pm 15.1°$
v_{land} (mean, $1-\sigma$)	8.68 ± 0.46 cm/s	5.0 ± 0.66 cm/s

Initially, a pointwise propagated trajectory is found using a simple single shooting approach, where the trajectory is propagated backward from the estimated DART crater location to the final time, minimizing the difference between the actual final position and the desired deployment location (assumed here to be located on the x axis of the synodic frame at 2.0 km away from the barycenter). This trajectory is then used as both a comparison against the robust method discussed here and as an initial guess for the NLP solver. The uncertainties considered here are 100 m ($3-\sigma$) in the deployment position, 5% ($3-\sigma$) in the velocity magnitude of the deployment and braking maneuver, and 3 deg ($3-\sigma$) in the pointing of the deployment and braking maneuver. The specific solver used here is the WORHP algorithm [62].

The results of an MC analysis of both the pointwise and robust approach are summarized in Table 3. The main result is the large increase in trajectories landing on Dimorphos, going from 74.3 to 99.8%. This is done by significantly reducing the magnitude of the maneuvers and at the same time changing the pointing slightly while keeping the braking time almost the same as for the pointwise result. This results in a smaller uncertainty set due to the proportionality of the Δv error and thus results in a significantly smaller landing ellipse, as can be seen in Fig. 17, and in significantly reducing the landing

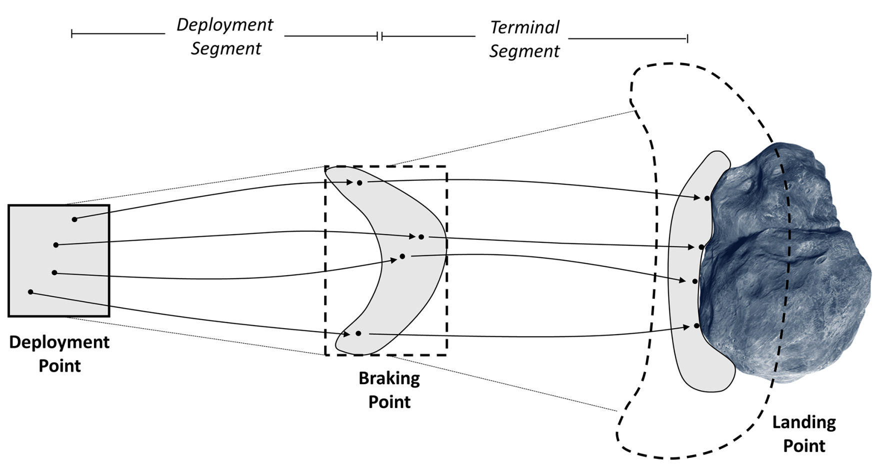

Fig. 16 Diagram explaining the robust landing trajectory optimization method.

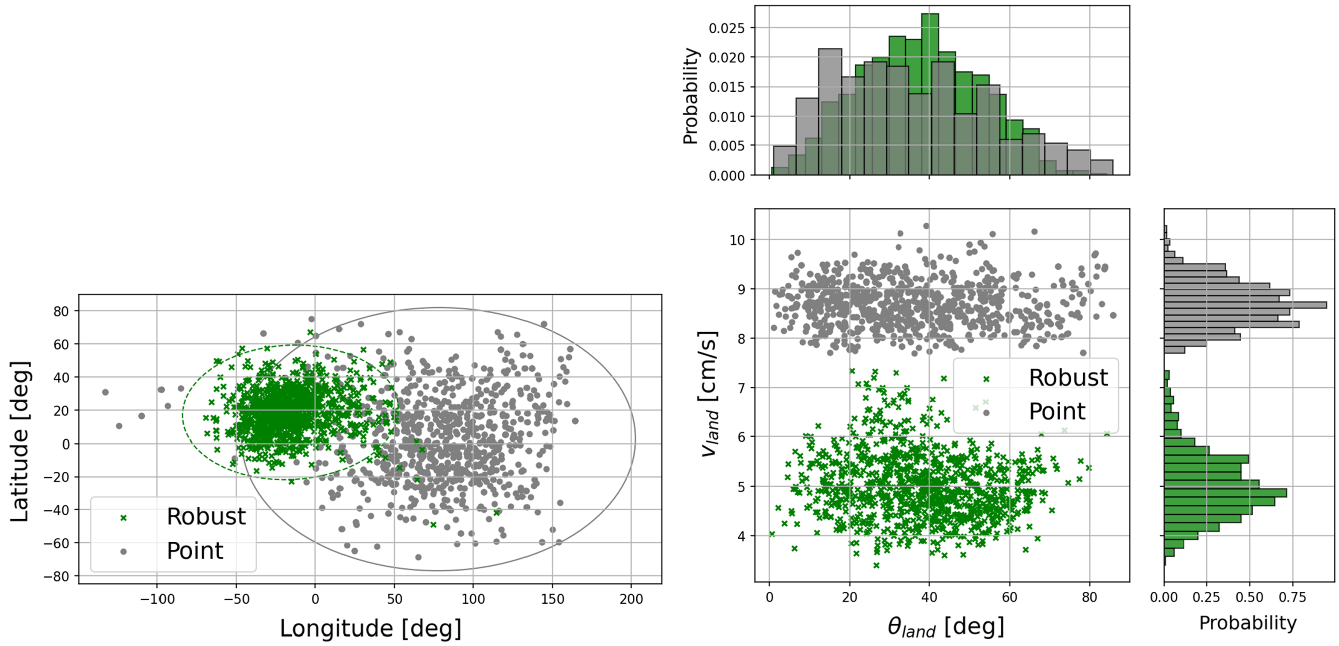

a) Landing location distribution and 3-σ ellipse

b) Landing geometry distribution

Fig. 17 The distributions of landing location and geometry of both the robust optimization method and the nominal pointwise method.

velocities, as shown in Fig. 17b. However, this does come at the cost of moving the mean landing location more away from the estimated crater location and also increasing the mean impact angle (see Table 3).

To determine how these results relate to the desired landing conditions found in Sec. IV, the MC results are projected on the $\tilde{\gamma}$ maps in Fig. 18. It can be seen that for both cases the trajectories of the robust solution are located in lower $\tilde{\gamma}$ regions compared to the pointwise solution. For the smooth case in Fig. 18a, the higher mean impact angle does not result in trajectories bouncing off the surface again, as the mean impact angle is sufficiently low to allow for all trajectories to settle on the surface. Similarly for the rocky case, the low sensitivity to this angle and the fact that the mean touchdown velocity is much lower in comparison to the nominal case result in the majority of the MC samples for the robust solution residing in low $\tilde{\gamma}$ regions, which directly relates to a high probability of a successful landing.

VII. Conclusions

This work introduces a novel methodology for the design and analysis of ballistic landing trajectories on the secondary of a binary asteroid. The methodology shows how efficient uncertainty propagation and quantification tools, specifically NCI and the pseudo-diffusion indicator, can be used to analyze the uncertain dynamics and design a robust landing trajectory.

It was shown how the pseudo-diffusion indicator can be used to determine constraints on the landing geometry and touchdown velocity that ensure high probability of the spacecraft settling on the surface of the asteroid. For the model where a smooth surface of the asteroid was assumed, a maximum touchdown velocity of 10 cm/s was found and a maximum impact angle of 20 deg. As the touchdown velocity decreases, the maximum allowable impact angle also increases, where for around 6 cm/s almost all impact angles result in settling on the surface. A transition region also appears for touchdown velocities between 10 and 6 cm/s and high impact angles,

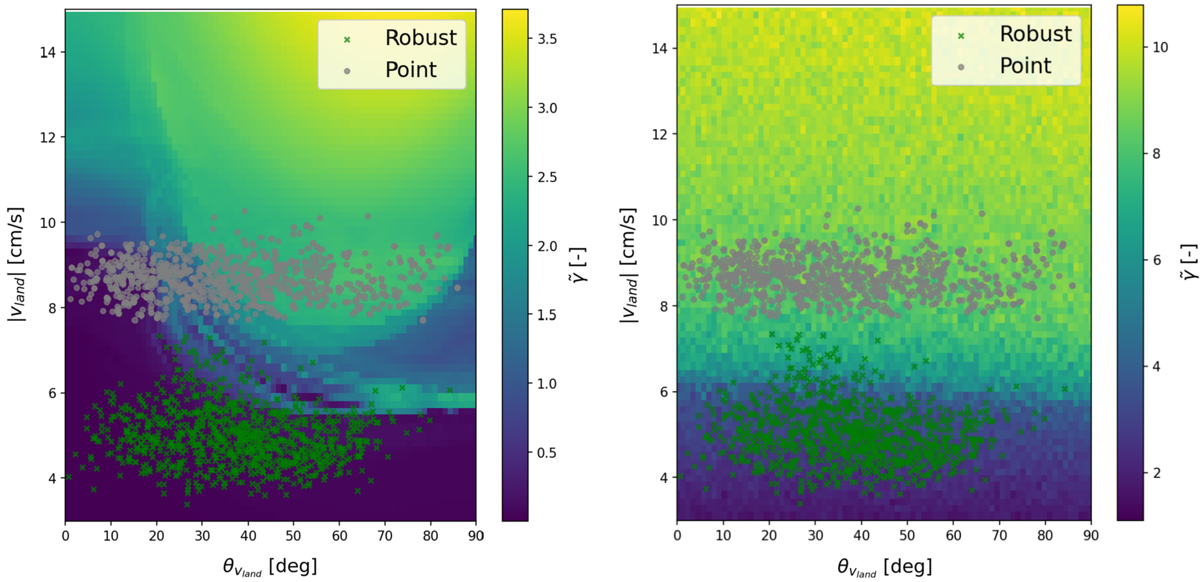

a) Smooth surface

b) Rocky surface

Fig. 18 Samples of both trajectory design methodologies projected in the $\tilde{\gamma}$ maps.

where part of the trajectories settle on Dimorphos's surface and part go into an orbit around the system. When the dynamics are altered to model surface features like rocks and craters using a stochastic perturbation on the local surface normal, the dependency on the impact angle is less significant and the maximum touchdown velocity decreases to around 8 cm/s.

Using an NCI-based bisection method, it was then found that if a landing location in the DART crater hemisphere is considered with a deployment point 2 km away from the system, the necessary minimum touchdown velocity would be much higher than what is required for settling on the surface. Thus, an extra braking maneuver is needed along the trajectory to reduce the touchdown velocity.

The deployment Δv, braking Δv, and time of the braking Δv were then determined using a novel method that incorporates the NCI uncertainty propagation method into the trajectory optimization transcription. This method was able to find a trajectory that increases the landing success percentage from 74.3 to 94.7% compared to a trajectory designed without considering the uncertainties. Furthermore, the landing footprint on Dimorphos was also significantly reduced, together with lowering the mean touchdown velocity. This comes at the cost of increasing the mean impact angle and moving the mean landing longitude away from the desired location. However, even with these changes, the robust trajectory was found to be much more desirable.

These results show the potential of this methodology for the design of a ballistic landing on Dimorphos. The increased knowledge about the uncertain and stochastic dynamics gained through the NCI and pseudo-diffusion indicator techniques increases the robustness and performance of these types of missions, and thus it is important to use them in the mission design process.

Acknowledgments

This research is funded by the European Space Agency's Open Space Innovation Platform, under contract number 4000130259/20/NL/MH/ac, "Bounded Stability of Motions Around Minor Bodies," with the University of Strathclyde. The authors would like to thank Onur Celik for his insights on the modeling of the surface motion and his ideas regarding this work. Furthermore, the authors would also like to thank the reviewers for their insightful comments.

References

[1] Michel, P., Küppers, M., Bagatin, A. C., Carry, B., Charnoz, S., De Leon, J., Fitzsimmons, A., Gordo, P., Green, S. F., Hérique, A., et al., "The ESA Hera Mission: Detailed Characterization of the DART Impact Outcome and of the Binary Asteroid (65803) Didymos," *Planetary Science Journal*, Vol. 3, No. 7, 2022, p. 160.
https://doi.org/10.3847/PSJ/ac6f52

[2] Cheng, A. F., Agrusa, H. F., Barbee, B. W., Meyer, A. J., Farnham, T. L., Raducan, S. D., Richardson, D. C., Dotto, E., Zinzi, A., Della Corte, V., et al., "Momentum Transfer from the DART Mission Kinetic Impact on Asteroid Dimorphos," *Nature*, Vol. 616, No. 7957, 2023, pp. 457–460.
https://doi.org/10.1038/s41586-023-05878-z

[3] Goldberg, H., Karatekin, O., Ritter, B., Herique, A., Tortora, P., Prioroc, C., Gutierrez, B., Martino, P., and Carnelli, I., "The Juventas CubeSat in Support of ESA's Hera Mission to the Asteroid Didymos," *33rd Annual AIAA/USU Conference on Small Satellites*, Utah State Univ. Space Dynamics Lab., Paper SSC19-WKIV-05, 2019, https://digitalcommons.usu.edu/smallsat/2019/all2019/73.

[4] Kawaguchi, J., "Hayabusa, Summary of Guidance, Navigation and Control Achievement in Its Proximity Phase," *Collection of Technical Papers - AIAA/AAS Astrodynamics Specialist Conference*, Vol. 2, AIAA Paper 2006-6533, 2006.
https://doi.org/10.2514/6.2006-6533

[5] Muñoz, P., Budnik, F., Companys, V., Godard, B., Casas, C. M., Morley, T., and Janarthanan, V., "Rosetta Navigation During Lander Delivery Phase and Reconstruction of Philae Descent Trajectory and Rebound," *25th International Symposium on Space Flight Dynamics*, DLR Space Operations, Paper ISSFD12-3, 2015.

[6] Tsuda, Y., Saiki, T., Terui, F., Nakazawa, S., Yoshikawa, M., and Watanabe, S. I., "Hayabusa2 Mission Status: Landing, Roving and Cratering on Asteroid Ryugu," *Acta Astronautica*, Vol. 171, June 2020, pp. 42–54.
https://doi.org/10.1016/j.actaastro.2020.02.035

[7] Lauretta, D. S., Balram-Knutson, S. S., Beshore, E., Boynton, W. V., Drouet, d'Aubigny, Enos, H. L., Golish, D. R., Hergenrother, C. W., Howell, E. S., Bennett, C. A., et al., "OSIRIS-REx: Sample Return from Asteroid (101955) Bennu," *Space Science Reviews*, Vol. 212, Nos. 1–2, 2017, pp. 925–984.
https://doi.org/10.1007/s11214-017-0405-1

[8] Çelik, O., Karatekin, O., Ritter, B., and Sánchez, J.-P., "Reliability Analysis of Ballistic Landing in Binary Asteroid 65803 (1996GT) Didymos under Uncertainty and GNC Error Considerations," *26th International Symposium on Spaceflight Dynamics*, Vol. ists14, Matsuyama, Japan, Paper a90510, June 2017

[9] Tardivel, S., and Scheeres, D. J., "Ballistic Deployment of Science Packages on Binary Asteroids," *Journal of Guidance, Control, and Dynamics*, Vol. 36, No. 3, 2013, pp. 700–709.
https://doi.org/10.2514/1.59106

[10] Tardivel, S., Michel, P., and Scheeres, D. J., "Deployment of a Lander on the Binary Asteroid (175706) 1996 FG3, Potential Target of the European MarcoPolo-R Sample Return Mission," *Acta Astronautica*, Vol. 89, Aug. 2013, pp. 60–70.
https://doi.org/10.1016/j.actaastro.2013.03.007

[11] Herrera-Sucarrat, E., Palmer, P. L., and Roberts, R. M., "Asteroid Observation and Landing Trajectories Using Invariant Manifolds," *Journal of Guidance Control and Dynamics*, Vol. 37, No. 3, 2014, pp. 907–920.
https://doi.org/10.2514/1.59594

[12] Villegas Pinto, D., Hestroffer, D., Canalias, E., and Capolupo, F., "Deployment of Small-Body Landers from Terminator Orbits in Perturbed Environments," *AAS/AIAA Astrodynamics Specialist Conference*, Paper AAS 20-728, 2020.

[13] Ferrari, F., and Lavagna, M., "Ballistic Landing Design on Binary Asteroids: The AIM Case Study," *Advances in Space Research*, Vol. 62, No. 8, 2018, pp. 2245–2260.
https://doi.org/10.1016/j.asr.2017.11.033

[14] Fodde, I., Feng, J., and Vasile, M., "Robust Trajectory Design for Ballistic Landings on Dimorphos," *AIAA Science and Technology Forum and Exposition, AIAA SciTech Forum 2022*, AIAA Paper 2022-1476, 2022.
https://doi.org/10.2514/6.2022-1476

[15] Sawai, S., Kawaguchi, J., Scheeres, D., Yoshizawa, N., and Ogasawara, M., "Development of a Target Marker for Landing on Asteroids," *Journal of Spacecraft and Rockets*, Vol. 38, No. 4, 2012, pp. 601–608.
https://doi.org/10.2514/2.3723

[16] Van Wal, S., Tardivel, S., and Scheeres, D., "Parametric Study of Ballistic Lander Deployment to Small Bodies," *Journal of Spacecraft and Rockets*, Vol. 54, No. 6, 2017, pp. 1330–1355.
https://doi.org/10.2514/1.A33832

[17] Van Wal, S., Reid, R. G., and Scheeres, D. J., "Simulation of Nonspherical Asteroid Landers: Contact Modeling and Shape Effects on Bouncing," *Journal of Spacecraft and Rockets*, Vol. 57, No. 1, 2019, pp. 109–130.
https://doi.org/10.2514/1.A34573

[18] Rusconi, M., Ferrari, F., and Topputo, F., "The Effect of a Rocky Terrain for CubeSat Landing on Asteroid Surfaces," *Advances in Space Research*, Vol. 71, No. 1, 2022, pp. 829–844.
https://doi.org/10.1016/J.ASR.2022.10.056

[19] Zeng, X. Y., Li, Z. W., Wen, T. G., and Zhang, Y. L., "Influence of the Lander Size and Shape on the Ballistic Landing Motion," *Earth and Space Science*, Vol. 9, No. 2, 2022, Paper e2021EA001952.
https://doi.org/10.1029/2021EA001952

[20] Feng, J., Hou, X., and Armellin, R., "Survey on Studies About Model Uncertainties in Small Body Explorations," *Progress in Aerospace Sciences*, Vol. 110, Oct. 2019, Paper 100549.
https://doi.org/10.1016/j.paerosci.2019.05.009

[21] Dunham, D. W., Farquhar, R. W., McAdams, J. V., Holdridge, M., Nelson, R., Whittenburg, K., Antreasian, P., Chesley, S., Helfrich, C., Owen, W. M., et al., "Implementation of the First Asteroid Landing," *Icarus*, Vol. 159, No. 2, 2002, pp. 433–438.
https://doi.org/10.1006/icar.2002.6911

[22] Greco, C., and Vasile, M., "Closing the Loop Between Mission Design and Navigation Analysis," *71th International Astronautical Congress (IAC 2020)*, International Astronautical Federation (IAF), Paris, France, Oct. 2020, pp. 1–13.

[23] Luo, J., Liu, Q., Yang, Y., Li, X., Chen, M.-R., and Cao, W., "An Artificial Bee Colony Algorithm for Multi-Objective Optimisation," *Applied Soft Computing Journal*, Vol. 50, Jan. 2017, pp. 235–251.
https://doi.org/10.1016/j.asoc.2016.11.014

[24] Vasile, M., and Manzi, M., "Polynomial Stochastic Dynamical Indicators," *Celestial Mechanics and Dynamical Astronomy*, Vol. 135, No. 1, 2023, pp. 1–35.
https://doi.org/10.1007/s10569-022-10116-1

[25] Richardson, D. C., Agrusa, H. F., Barbee, B., Bottke, W. F., Cheng, A. F., Eggl, S., Ferrari, F., Hirabayashi, M., Karatekin, O., McMahon, J., et al., "Predictions for the Dynamical States of the Didymos System Before and After the Planned DART Impact," *Planetary Science Journal*, Vol. 3, No. 7, 2022, p. 157.
https://doi.org/10.3847/PSJ/ac76c9

[26] "Hera Didymos Reference Model Issue 5," ESA Headquarters, ESA-TECSP-AD-017258, Paris, France, 2020.

[27] Cheng, A., Agrusa, H., Barbee, B., Meyer, A., Farnham, T., Raducan, S., Richardson, D., Dotto, E., Zinzi, A., Corte, V., et al., "Momentum Transfer from the DART Mission Kinetic Impact on Asteroid Dimorphos," *Nature*, Vol. 616, No. 7957, 2022, pp. 457–460.
https://doi.org/10.21203/rs.3.rs-2339073/v1

[28] Wakker, K., *Fundamentals of Astrodynamics*, Institutional Repository Delft Univ. of Technology, Delft, The Netherlands, 2015, Chap. 3.

[29] Ferrari, F., Franzese, V., Pugliatti, M., Giordano, C., and Topputo, F., "Trajectory Options for Hera's Milani CubeSat Around (65803) Didymos," *Journal of the Astronautical Sciences*, Vol. 68, No. 4, 2021, pp. 1–22.
https://doi.org/10.1007/s40295-021-00282-z

[30] Montenbruck, O., and Gill, E., *Satellite Orbits: Models, Methods and Applications*, Springer, Berlin, 2000, Chap. 3.
https://doi.org/10.1007/978-3-642-58351-3

[31] Scheeres, D. J., *Orbital Motion in Strongly Perturbed Environments*, Springer, Berlin, 2012, p. 43.
https://doi.org/10.1007/978-3-642-03256-1

[32] Balmino, G., "Gravitational Potential Harmonics from the Shape of an Homogeneous Body," *Celestial Mechanics & Dynamical Astronomy*, Vol. 60, No. 3, 1994, pp. 331–364.
https://doi.org/10.1007/BF00691901

[33] Vasile, M., Absil, C. O., and Riccardi, A., "Set Propagation in Dynamical Systems with Generalised Polynomial Algebra and Its Computational Complexity," *Communications in Nonlinear Science and Numerical Simulation*, Vol. 75, Aug. 2019, pp. 22–49.
https://doi.org/10.1016/j.cnsns.2019.03.019

[34] Greco, C., Campagnola, S., and Vasile, M., "Robust Space Trajectory Design Using Belief Optimal Control," *Journal of Guidance, Control, and Dynamics*, Vol. 45, No. 6, 2022, pp. 1060–1077.
https://doi.org/10.2514/1.G005704

[35] Press, W. H., Teukolsky, S. A., Vetterling, W. T., and Flannery, B. P., *Numerical Recipes 3rd Edition: The Art of Scientific Computing*, 3rd ed., Cambridge Univ. Press, Cambridge, MA, 2007, Chap. 5.

[36] Riccardi, A., Tardioli, C., and Vasile, M., "An Intrusive Approach to Uncertainty Propagation in Orbital Mechanics Based on Tchebycheff Polynomial Algebra," Advances in the Astronautical Sciences, Vol. 156, Univelt Inc, Vail, 2016, pp. 707–722.

[37] Fodde, I., Feng, J., and Vasile, M., "Uncertainty Propagation for Orbital Motion Around an Asteroid Using Generalized Intrusive Polynomial Algebra: Application to Didymos System," *8th International Conference on Astrodynamics Tools and Techniques*, ESA, Paper 343, 2021, https://pureportal.strath.ac.uk/en/publications/uncertainty-propagation-for-orbital-motion-around-an-asteroid-usi.

[38] Smolyak, S. A., "Quadrature and Interpolation Formulas for Tensor Products of Certain Classes of Functions," *Doklady Akademii Nauk SSSR*, Vol. 148, No. 5, 1963, pp. 1042–1045.

[39] Haller, G., and Sapsis, T., "Lagrangian Coherent Structures and the Smallest Finite-Time Lyapunov Exponent," *Chaos: An Interdisciplinary Journal of Nonlinear Science*, Vol. 21, No. 2, 2011, Paper 023115.
https://doi.org/10.1063/1.3579597

[40] Froeschlé, C., Lega, E., and Gonczi, R., "Fast Lyapunov Indicators. Application to Asteroidal Motion," *Celestial Mechanics and Dynamical Astronomy*, Vol. 67, No. 1, 1997, pp. 41–62.
https://doi.org/10.1023/A:1008276418601

[41] Feng, J., Hou, X., Di Lizia, P., Armellin, R., and Santeramo, D., "Sensitivity Analysis of the Orbital Motion Around 469219 Kamo'oalewa (2016 HO3) to Uncertainties on Asteroid Mass and Solar Radiation Pressure," *Advances in Space Research*, Vol. 69, No. 3, 2021, pp. 1602–1618.
https://doi.org/10.1016/J.ASR.2021.11.035

[42] Fodde, I., Feng, J., and Vasile, M., "Uncertainty Maps for Motion Around Binary Asteroids," *Celestial Mechanics and Dynamical Astronomy*, Vol. 134, No. 5, 2022, pp. 1–23.
https://doi.org/10.1007/s10569-022-10096-2

[43] Manzi, M., and Topputo, F., "A Flow-Informed Strategy for Ballistic Capture Orbit Generation," *Celestial Mechanics and Dynamical Astronomy*, Vol. 133, Nos. 11–12, 2021, pp. 1–16.
https://doi.org/10.1007/s10569-021-10048-2

[44] Alves, S. B., De Oliveira, G. F., De Oliveira, L. C., Passerat De Silans, T., Chevrollier, M., Oriá, M., and Cavalcante, H. L. S., "Characterization of Diffusion Processes: Normal and Anomalous Regimes," *Physica A: Statistical Mechanics and Its Applications*, Vol. 447, April 2016, pp. 392–401.
https://doi.org/10.1016/j.physa.2015.12.049

[45] Tardivel, S., Scheeres, D. J., Michel, P., Van Wal, S., and Sánchez, P., "Contact Motion on Surface of Asteroid," *Journal of Spacecraft and Rockets*, Vol. 51, No. 6, 2014, pp. 1857–1871.
https://doi.org/10.2514/1.A32939

[46] Kikuchi, S., Ogawa, N., Mori, O., Saiki, T., Takei, Y., Terui, F., Ono, G., Mimasu, Y., Yoshikawa, K., Van Wal, S., et al., "Ballistic Deployment of the Hayabusa2 Artificial Landmarks in the Microgravity Environment of Ryugu," *Icarus*, Vol. 358, April 2021, Paper 114220.
https://doi.org/10.1016/j.icarus.2020.114220

[47] Van wal, S., and Tardivel, S., "Effects of Restitution, Friction, and Attitude on 2D Low-Velocity Rigid-Body Impacts," *Advances in Space Research*, Vol. 67, No. 1, 2021, pp. 411–435.
https://doi.org/10.1016/j.asr.2020.09.046

[48] Van wal, S., Çelik, O., Tsuda, Y., Yoshikawa, K., and Kawakatsu, Y., "Reduced-Gravity Experiments of Nonspherical Rigid-Body Impact on Hard Surfaces," *Advances in Space Research*, Vol. 67, No. 1, 2021, pp. 436–476.
https://doi.org/10.1016/j.asr.2020.10.018

[49] Van wal, S., Tsuda, Y., Yoshikawa, K., Miura, A., Tanaka, S., and Scheeres, D., "Prearrival Deployment Analysis of Rovers on Hayabusa2 Asteroid Explorer," *Journal of Spacecraft and Rockets*, Vol. 55, No. 4, 2018, pp. 797–817.
https://doi.org/10.2514/1.A34157

[50] Çelik, O., Baresi, N., Ballouz, R. L., Ogawa, K., Wada, K., and Kawakatsu, Y., "Ballistic Deployment from Quasi-Satellite Orbits Around Phobos Under Realistic Dynamical and Surface Environment Constraints," *Planetary and Space Science*, Vol. 178, Nov. 2019, Paper 104693.
https://doi.org/10.1016/J.PSS.2019.06.010

[51] Biele, J., Ulamec, S., Maibaum, M., Roll, R., Witte, L., Jurado, E., Muñoz, P., Arnold, W., Auster, H. U., Casas, C., et al., "The Landing(s) of Philae and Inferences About Comet Surface Mechanical Properties," *Science*, Vol. 349, No. 6247, 2015, Paper aaa9816.
https://doi.org/10.1126/science.aaa9816

[52] Yano, H., Kubota, T., Miyamoto, H., Okada, T., Scheeres, D., Takagi, Y., Yoshida, K., Abe, M., Abe, S., Barnouin-Jha, O., et al., "Touchdown of the Hayabusa Spacecraft at the Muses Sea on Itokawa," *Science*, Vol. 312, No. 5778, 2006, pp. 1350–1353.
https://doi.org/10.1126/science.1126164

[53] Biele, J., Kesseler, L., Grimm, C. D., Schröder, S., Mierheim, O., Lange, M., and Ho, T.-M., "Experimental Determination of the Structural Coefficient of Restitution of a Bouncing Asteroid Lander," 2017, http://arxiv.org/abs/1705.00701.

[54] Scholten, F., Preusker, F., Elgner, S., Matz, K. D., Jaumann, R., Biele, J., Hercik, D., Auster, H. U., Hamm, M., Grott, M., et al., "The Descent and Bouncing Path of the Hayabusa2 Lander MASCOT at Asteroid (162173) Ryugu," *Astronomy & Astrophysics*, Vol. 632, Dec. 2019, Paper L3.
https://doi.org/10.1051/0004-6361/201936757

[55] Chesley, S. R., French, A. S., Davis, A. B., Jacobson, R. A., Brozović, M., Farnocchia, D., Selznick, S., Liounis, A. J., Hergenrother, C. W., Moreau, M. C., et al., "Trajectory Estimation for Particles Observed in the Vicinity of (101955) Bennu," *Journal of Geophysical Research: Planets*, Vol. 125, No. 9, 2020, Paper e2019JE006363.
https://doi.org/10.1029/2019JE006363

[56] Thuillet, F., Zhang, Y., Michel, P., Biele, J., Kameda, S., Sugita, S., Tatsumi, E., Schwartz, S. R., and Ballouz, R. L., "Numerical Modeling of Lander Interaction with a Low-Gravity Asteroid Regolith Surface - II. Interpreting the Successful Landing of Hayabusa2 MASCOT," *Astronomy & Astrophysics*, Vol. 648, July 2021, Paper A56.
https://doi.org/10.1051/0004-6361/201936128

[57] Moreno, F., Bagatin, A. C., Tancredi, G., Li, J. Y., Rossi, A., Ferrari, F., Hirabayashi, M., Fahnestock, E., Maury, A., Sandness, R., et al., "Characterization of the Ejecta from the NASA/DART Impact on Dimorphos: Observations and Monte Carlo Models," *Planetary Science Journal*, Vol. 4, No. 8, 2023, p. 138.
https://doi.org/10.3847/PSJ/ace827

[58] Miller, J. K., Konopliv, A. S., Antreasian, P. G., Bordi, J. J., Chesley, S., Helfrich, C. E., Owen, W. M., Wang, T. C., Williams, B. G., Yeomans, D. K., et al., "Determination of Shape, Gravity, and Rotational State of Asteroid 433 Eros," *Icarus*, Vol. 155, No. 1, 2002, pp. 3–17.
https://doi.org/10.1006/icar.2001.6753

[59] Michikami, T., Honda, C., Miyamoto, H., Hirabayashi, M., Hagermann, A., Irie, T., Nomura, K., Ernst, C. M., Kawamura, M., Sugimoto, K., et al., "Boulder Size and Shape Distributions on Asteroid Ryugu," *Icarus*, Vol. 331, Oct. 2019, pp. 179–191.
https://doi.org/10.1016/j.icarus.2019.05.019

[60] Çelik, O., and Sánchez, J. P., "Opportunities for Ballistic Soft Landing in Binary Asteroids," *Journal of Guidance, Control, and Dynamics*, Vol. 40, No. 6, 2017, pp. 1390–1402.
https://doi.org/10.2514/1.G002181

[61] Greco, C., Di Carlo, M., Vasile, M., and Epenoy, R., "Direct Multiple Shooting Transcription with Polynomial Algebra for Optimal Control Problems Under Uncertainty," *Acta Astronautica*, Vol. 170, May 2020, pp. 224–234.
https://doi.org/10.1016/j.actaastro.2019.12.010

[62] Büskens, C., and Wassel, D., "The ESA NLP Solver WORHP," *Modeling and Optimization in Space Engineering*, edited by G. Fasano, and J. D. Pintér, Vol. 73, Springer, New York, 2013, pp. 85–110.
https://doi.org/10.1007/978-1-4614-4469-5

J. McMahon
Associate Editor